ARTICLES
https://doi.org/10.1038/s41558-020-00972-w

nature climate change

Check for updates

Global terrestrial water storage and drought severity under climate change

Yadu Pokhrel[1]✉, Farshid Felfelani[1], Yusuke Satoh[2,3], Julien Boulange[2], Peter Burek[3], Anne Gädeke[4], Dieter Gerten[4,5], Simon N. Gosling[6], Manolis Grillakis[7], Lukas Gudmundsson[8], Naota Hanasaki[2], Hyungjun Kim[9], Aristeidis Koutroulis[7], Junguo Liu[10], Lamprini Papadimitriou[11], Jacob Schewe[4], Hannes Müller Schmied[12,13], Tobias Stacke[14], Camelia-Eliza Telteu[12], Wim Thiery[8,15], Ted Veldkamp[3,16,17], Fang Zhao[18] and Yoshihide Wada[3,17]

Terrestrial water storage (TWS) modulates the hydrological cycle and is a key determinant of water availability and an indicator of drought. While historical TWS variations have been increasingly studied, future changes in TWS and the linkages to droughts remain unexamined. Here, using ensemble hydrological simulations, we show that climate change could reduce TWS in many regions, especially those in the Southern Hemisphere. Strong inter-ensemble agreement indicates high confidence in the projected changes that are driven primarily by climate forcing rather than land and water management activities. Declines in TWS translate to increases in future droughts. By the late twenty-first century, the global land area and population in extreme-to-exceptional TWS drought could more than double, each increasing from 3% during 1976–2005 to 7% and 8%, respectively. Our findings highlight the importance of climate change mitigation to avoid adverse TWS impacts and increased droughts, and the need for improved water resource management and adaptation.

Terrestrial water storage (TWS)—the sum of continental water stored in canopies, snow and ice, rivers, lakes and reservoirs, wetlands, soil and groundwater—is a critical component of the global water and energy budget. It plays key roles in determining water resource availability[1] and modulating water flux interactions among various Earth system components[2]. Further, TWS changes are inherently linked to droughts[2–6], floods[7] and global sea level change[8–11]. Despite such importance, global TWS remains less studied relative to hydrological fluxes (for example, river discharge, evapotranspiration and groundwater flow) owing to the lack of large-scale observations and challenges in explicitly resolving all TWS components in hydrological modelling[12]. This generally holds true for historical analyses; crucially, no study has to date examined the potential impacts of future climate change on global TWS.

Recent modelling advancements[13] have improved the representation of TWS in global hydrological models[14,15] (GHMs) and land surface models[12] (LSMs). The Gravity Recovery and Climate Experiment (GRACE) satellite mission provided added opportunities to improve and validate TWS simulations in these models. GRACE TWS data and model simulations, often in combination, have been used for wide-ranging applications including the assessment of water resources and impacts of human activities on the water cycle[14,16], quantifying aquifer depletion[12,14,17–19], monitoring drought[3–6,20] and assessing flood potential[7]. These studies have advanced the understanding of global TWS systems that are continually changing under natural hydroclimatic variability and accelerating land and water management activities, but the focus has been on historical variabilities in TWS. Further, future projections from general circulation models (GCMs) have been used to quantify climate change impacts on hydrological fluxes[21–23] and storages, but the projections of storages are limited to a subset of TWS components—specifically soil moisture and snow[24–26]—owing to an incomplete representation of TWS components in the GCMs. Lack of explicit parameterizations for surface water and groundwater processes and use of shallow rooting depth in GCMs have particularly hindered comprehensive TWS projections using GCM simulations[25].

As TWS represents the total water availability on land, it also provides an integrated measure of the overall drought condition in a region[5,6]. Drought—a slow-evolving phenomenon—is among the costliest natural disasters[27], directly affecting water resources, agriculture, socioeconomic development and ecosystem health and often linked with armed conflicts[28]. Substantial literature exists on the study of droughts using indices such as the standardized

[1]Department of Civil and Environmental Engineering, Michigan State University, East Lansing, MI, USA. [2]National Institute for Environmental Studies, Tsukuba, Japan. [3]International Institute for Applied Systems Analysis, Laxenburg, Austria. [4]Potsdam Institute for Climate Impact Research (PIK), Potsdam, Germany. [5]Geography Department, Humboldt-Universität zu Berlin, Berlin, Germany. [6]School of Geography, University of Nottingham, Nottingham, UK. [7]School of Environmental Engineering, Technical University of Crete, Chania, Greece. [8]Institute for Atmospheric and Climate Science, ETH Zurich, Zurich, Switzerland. [9]Institute of Industrial Science, The University of Tokyo, Tokyo, Japan. [10]School of Environmental Science and Engineering, Southern University of Science and Technology, Shenzhen, China. [11]Cranfield Water Science Institute (CWSI), Cranfield University, Cranfield, UK. [12]Institute of Physical Geography, Goethe-University Frankfurt, Frankfurt am Main, Germany. [13]Senckenberg Leibniz Biodiversity and Climate Research Centre Frankfurt (SBiK-F), Frankfurt am Main, Germany. [14]Institute of Coastal Research, Helmholtz-Zentrum Geesthacht (HZG), Geesthacht, Germany. [15]Department of Hydrology and Hydraulic Engineering, Vrije Universiteit Brussel, Brussels, Belgium. [16]Department of Water & Climate Risk, VU University, Amsterdam, the Netherlands. [17]Department of Physical Geography, Utrecht University, Utrecht, the Netherlands. [18]School of Geographic Sciences, East China Normal University, Shanghai, China. ✉e-mail: ypokhrel@egr.msu.edu

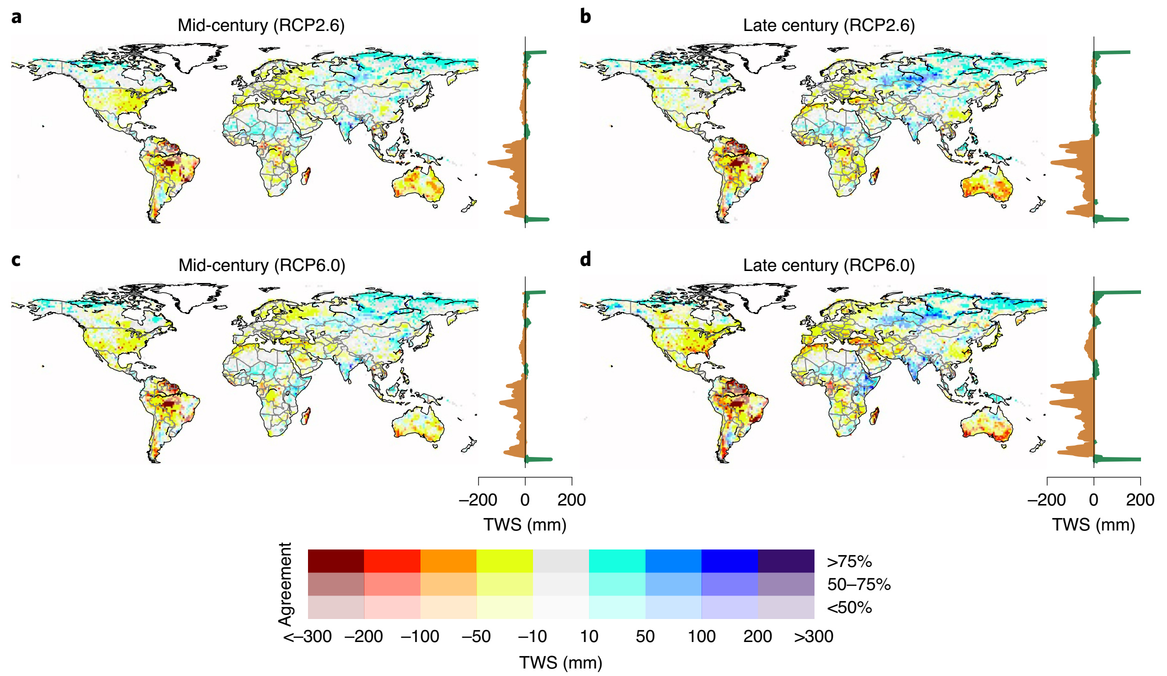

Fig. 1 | Impact of climate change on TWS. a–d, The changes (multi-model weighted mean) in TWS, averaged for the mid- (2030–2059; **a**,**c**) and the late (2070–2099; **b**,**d**) twenty-first century under RCP2.6 (**a**,**b**) and RCP6.0 (**c**,**d**) relative to the average for the historical baseline period (1976–2005). The colour hues show the magnitude of change and the saturation indicates the agreement, among ensemble members, in the sign of change. The graph on the right of each panel shows the latitudinal mean.

precipitation index (SPI)[29], Palmer drought severity index[30], soil moisture drought index (SMI)[31,32] and standardized runoff index (SRI)[33]. These conventional indices have been used in monitoring and projecting[32,34] meteorological, agricultural and hydrological droughts[35]. Recently, a new drought index, the TWS drought severity index (TWS-DSI[5]), has been employed to examine droughts[36,37] in relation to the vertically integrated water storage as opposed to the individual storages or fluxes used in conventional indices. Previous studies[5,36,37] have demonstrated that the TWS-DSI correlates with the conventional indices in regions with long-term water storage change but provides an integrated measure, especially by capturing the effects of slow-responding terms (such as deep soil moisture and groundwater). Further, an increasing number of TWS-based drought studies have shown that combining TWS with traditional drought indices can provide crucial insights into drought impacts on hydrologic systems and vegetation growth[6,36,37], because TWS directly responds to changes in precipitation, integrates soil moisture and modulates runoff generation, hence encompassing the three aforementioned drought types[36]. However, as previous TWS studies have focused on historical droughts[3–6,20], the changes in future droughts due to TWS change and variability remain unexamined.

Here we present a global assessment of the impacts of future climate change on TWS. We then examine the changes in drought severity and frequency resulting from climate-induced TWS change and variability by using the monthly TWS-DSI[5] (see Methods and Supplementary Table 1). We use multi-model hydrological simulations (27 ensemble members; Supplementary Table 2) from seven terrestrial hydrology models (LSMs and GHMs; Supplementary Table 3) driven by atmospheric forcing from four GCMs (see Methods). Four cases of radiative forcing are considered for each GCM: the pre-industrial control (PIC), historical climate (HIST), and low (Representative Concentration Pathway (RCP)2.6) and medium–high (RCP6.0) emission scenarios (see Methods). Simulations are conducted under the framework of the Inter-Sectoral Impact Model Intercomparison Project, phase 2b (ISIMIP2b[38]; https://www.isimip.org/). We use the multi-model weighted mean of TWS anomalies, calculated by weighting the ensemble members on the basis of their continent-level skill and independence scores[39] (Methods and Extended Data Figs. 1 and 2).

TWS under climate change

By the mid- (2030–2059) and late (2070–2099) twenty-first century, TWS is projected to substantially decline in the majority of the Southern Hemisphere, the conterminous United States, most of Europe and the Mediterranean, but increase in eastern Africa, south Asia and northern high latitudes, especially northern Asia (Fig. 1). The latitudinal mean (Fig. 1) indicates a larger decline in TWS in the Southern Hemisphere than in the Northern Hemisphere, driven primarily by the decline in South America and Australia; this is in line with the projected precipitation changes (Extended Data Fig. 3) and could partly be due to a tendency of GCMs to overestimate[27] drying trends in the Southern Hemisphere. The changes are evident by the mid-twenty-first century (under both RCPs; Fig. 1a,c), but the signal becomes stronger by the late twenty-first century, especially under RCP6.0 (Fig. 1d). Exceptions are found in parts of the conterminous United States, where TWS under RCP2.6 is projected to decline by mid-century but then increase slightly thereafter, owing to the projected increase in precipitation across most of the region (Extended Data Fig. 3) combined with a decrease in temperature from the mid- to the late twenty-first century (Extended Data Fig. 4). For RCP6.0, the projected changes (positive or negative) seen during mid-century become more pronounced later for most global regions. The differences between the two RCPs are, however, less obvious for both periods; an exception is Australia where the spatial extent of decline in TWS is projected to be smaller under RCP6.0 than under RCP2.6 (Fig. 1), which aligns with wetter conditions projected in RCP6.0 (Extended Data Fig. 3). Globally, TWS declines (increases) in 67% (33%) of land area (excluding Greenland, Antarctica and glaciers) by the late twenty-first century under RCP6.0.

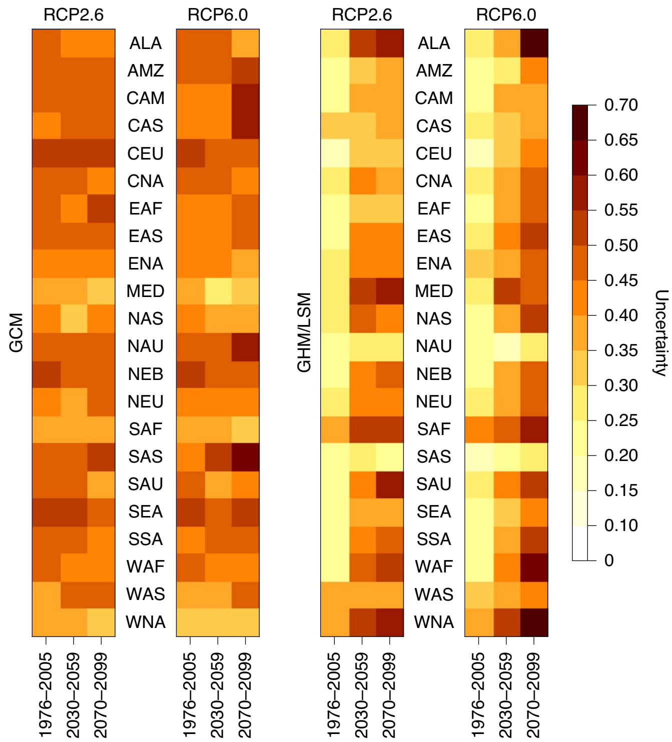

Fig. 2 | Uncertainty in TWS simulations. Contributions of GCMs and GHMs/LSMs to the uncertainty in TWS simulations (the range statistic of the quantile-based TWS index; see Methods), averaged over the sub-continental regions defined by the IPCC SREX (a description of the regions is provided in Supplementary Fig. 3). The horizontal axis denotes the historical baseline period (1976–2005) and the mid- (2030–2059) and late (2070–2099) twenty-first century. A lighter colour marks a smaller variability in TWS simulations across GCMs or GHMs/LSMs. CEU, central Europe; EAS, east Asia; ENA, East North America; NEB, Northeast Brazil; NEU, north Europe; SEA, Southeast Asia.

Overall, strong agreement is found across ensemble members in the sign of change (colour saturation in Fig. 1), indicating high confidence in the projections. For the late twenty-first century, an agreement of >50% can be seen in regions where a large decline or increase in TWS is projected; such agreement is >75% for regions such as the Amazon basin, southern Australia, the Mediterranean and the eastern United States (Fig. 1). This confidence is reinforced by the good agreement between the simulated TWS and GRACE data for the historical period (Extended Data Fig. 5 and Supplementary Figs. 1 and 2). The broad global spatial patterns and seasonal variations in TWS are accurately captured by the multi-model ensemble mean, although some differences are evident in the magnitude of the seasonal amplitude (Extended Data Fig. 5). Such differences stand out especially along major river channels (such as the Amazon, Nile and Mississippi) that are explicitly considered in the models but not resolved in the GRACE data. Further, the seasonal dynamics and interannual variability in the simulated TWS averaged over the major global river basins also agree reasonably well with the GRACE data (Supplementary Figs. 1 and 2), even though there are some disagreements between the trend in GRACE and the multi-model mean (Supplementary Fig. 2), probably due to uncertainties in model parameterizations and potential biases in GCM-based forcing data.

Uncertainty in TWS simulations

The inter-ensemble spread in TWS simulations is a combination of the uncertainties arising from climate forcing (driven by GCMs) and GHM/LSM parameterizations (see Methods). The GCM uncertainty (for a given RCP scenario) is larger than the GHM/LSM uncertainty in most regions for the historical period and mid-twenty-first century (Fig. 2). However, the GHM/LSM uncertainty increases substantially with time, leading to a higher GHM/LSM uncertainty in most regions by the late twenty-first century, especially under RCP6.0. The GHM/LSM uncertainty range (Fig. 2, two right panels) for the historical period is relatively small, consistent with good agreement of the seasonal amplitude and temporal variability of TWS with GRACE data (Extended Data Fig. 5 and Supplementary Figs. 1 and 2), which probably reflects the relative benefits of bias correction using observations for the same period.

Regional variability and seasonality in TWS projections

The projected changes in the seasonal cycle of TWS vary spatially among regions defined by the Intergovernmental Panel on Climate Change (IPCC) Special Report On Extremes (SREX) (Fig. 3 and Supplementary Fig. 3). The Amazon (AMZ), South Europe/Mediterranean (MED), North Australia (NAU), Northeast Brazil, South Australia/New Zealand (SAU), Southeastern South America (SSA) and West Africa (WAF) are projected to experience a decline in TWS across all seasons. In Alaska (ALA), a slight increase is observed during winter months—probably due to an increase in snow amount—but a discernible decline is seen during summer-to-autumn months, potentially caused by a warming-driven increase in evapotranspiration. In regions where TWS is expected to increase, changes in the seasonal cycle vary. While South Asia (SAS) could experience an increase in TWS across all seasons, increases are projected only during late autumn to early spring in North Asia (NAS); in East Africa (EAF), increases are expected in all seasons but only under RCP6.0. Many of the regions projected to experience an increase in TWS overlap with regions with higher future precipitation (Extended Data Fig. 3). We find the strong drying in MED to be consistent with the historically observed north (wet)–south (dry) contrast in pan-European river flows[40], implying that the regions with historical drying trends are expected to become even drier under climate change. Our results for AMZ also corroborate the widely discussed drying and lengthening of the dry season[41], suggesting that the findings are robust for this region and add to the long-standing debate on the fate of the Amazonian rainforest under a warmer, drier future[42].

Soil moisture has been used previously as an indicator of total TWS, on the basis that its variability constitutes a large portion of the total TWS variability[26]. We find that the component contribution ratio (CCR; Methods) of soil moisture to total TWS varies substantially among SREX regions. Generally, soil moisture contribution is high (>50%) in relatively dry regions, including Central America/Mexico (CAM), MED, West Asia (WAS), Central Asia (CAS), WAF, Southern Africa (SAF) and SAU, and low in relatively humid and snow-dominated regions including ALA, NAS and AMZ (Extended Data Fig. 6), as also noted by previous studies[16,43]. The results suggest that soil moisture could not be used to substitute TWS globally.

Changes in TWS are driven primarily by climate forcing, as opposed to land and water management and/or socioeconomic drivers (see Methods). This is apparent from comparing the HIST and RCP simulations with the PIC simulations (see Methods) for the baseline period and late twenty-first century (Fig. 3). As the PIC simulations use identical socioeconomic scenarios as the HIST and RCP simulations for the respective periods (Supplementary Table 2), the PIC (2070–2099) versus PIC (1976–2005) comparison suggests that TWS would have remained generally stable in most regions under a pre-industrial climate. Differences between the two simulations can, however, be seen in some regions (for example, EAF, SSA and WAS) even though the difference in the global average is relatively small (Fig. 3). Globally, this difference is ~11% of the difference between RCP6.0 (2070–2099) and PIC (1976–2005),

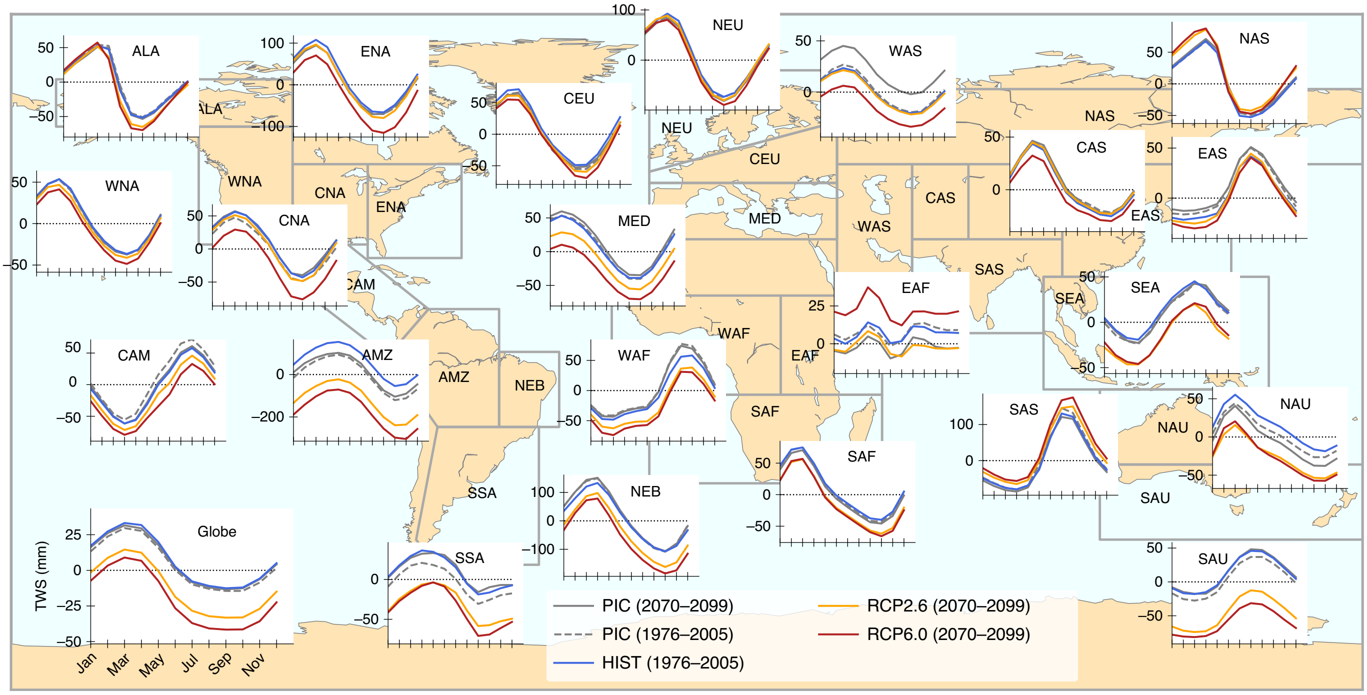

Fig. 3 | Seasonal TWS variations averaged over the selected IPCC SREX regions. The seasonal cycle (weighted mean; the same continental weights are used for all simulations) is estimated from the TWS time series for the respective periods (see legends), but the anomalies are calculated by using the mean for the 1861–2099 period, generated by combining the results from HIST simulations with the corresponding RCP scenario. The labels and unit are shown in the inset for the entire globe. A description of the SREX regions is provided in Supplementary Fig. 3.

meaning that ~90% of the projected change could be attributed to climate change. A decrease in TWS is projected under pre-industrial climate in CAM, EAF and NAU. Other regions including Central North America (CNA), AMZ, SSA, WAS and SAU would have been wetter in the future under pre-industrial climate. These results suggest that while the wetting caused by climate change could be offset by land and water management and socioeconomic drivers in some regions (such as EAF), the climate-induced drying could be further exacerbated by human activities in others (including NAU).

Future projection of TWS drought

The projected changes in TWS correspond with shifts in future drought occurrence and severity. Many regions are projected to experience an increased occurrence of moderate-to-severe ($-0.8 \leq$ TWS-DSI < -1.6) and extreme-to-exceptional (TWS-DSI ≤ -1.6; see Methods and Supplementary Table 1) TWS droughts (Fig. 4a,b). The direction of change is robust among ensemble members, especially in regions that are projected to experience an increase in the number of drought days (for example the Amazon river basin, Mediterranean, conterminous United States, east Asia and parts of Australia). By the late twenty-first century (RCP6.0), the frequency of moderate, severe, extreme and exceptional TWS droughts is projected to increase substantially (17–34%; Supplementary Table 4) in all continents but Asia (Fig. 4c,e–h). This is caused largely by a notable reduction in the frequency of near-normal to abnormally dry and slightly wet conditions in Africa and North America, primarily of wet conditions in Europe, and of near-normal and wet conditions in South America and Australia. Further, results suggest a general reduction in the frequency of wet conditions globally except in Asia and, to some extent, in Africa. Asia stands out among all continents where the frequency of severe, extreme and exceptional droughts as well as that of moderately wet to exceptionally wet conditions is projected to increase, caused by a reduced frequency of near-normal and slightly dry and wet conditions (Fig. 4d).

Global land area and projected future population (see Methods) exposed to moderate-to-severe TWS drought are projected to increase steadily until the mid-twenty-first century and remain relatively stable during the late twenty-first century. However, those under extreme-to-exceptional TWS drought are projected to increase until the end of the century (Fig. 4i,j) with a noticeable increase in inter-ensemble spread towards the late century, consistent with the increase in GHM/LSM uncertainty (Fig. 2). Under RCP6.0, both the global land area and projected population in moderate-to-severe TWS drought increase from 15% during the baseline period of 1976–2005 to 18% and 20%, respectively, by the mid- and late twenty-first century. This change in population translates to an additional ~600 and ~859 million people, respectively. From the mid- to the late twenty-first century, the global population in moderate-to-severe TWS drought for at least 30 days per year increases from 59% to 63%, and the population experiencing at least 60 days per year increases from 45% to 49%. For extreme-to-exceptional TWS drought under RCP6.0, land area increases from a 3% baseline to 4% and 7% during the mid- and late twenty-first century, respectively. The population exposed to these conditions increases from a baseline of 3% to 4% and 8%, or an additional ~154 and ~488 million people. The population exposed to at least 30 days of extreme-to-exceptional TWS drought increases from 19% to 27%, and at least 60 days from 11% to 18%, between the mid- and late twenty-first century.

At the regional scale, the frequency of extreme and exceptional TWS droughts is projected to increase by the late twenty-first century in most SREX regions (Fig. 5 and Methods). The changes in drought frequency are evident under both RCPs but are generally more pronounced under RCP6.0. Overall, the probability density functions (PDFs) characterized by a symmetrical distribution

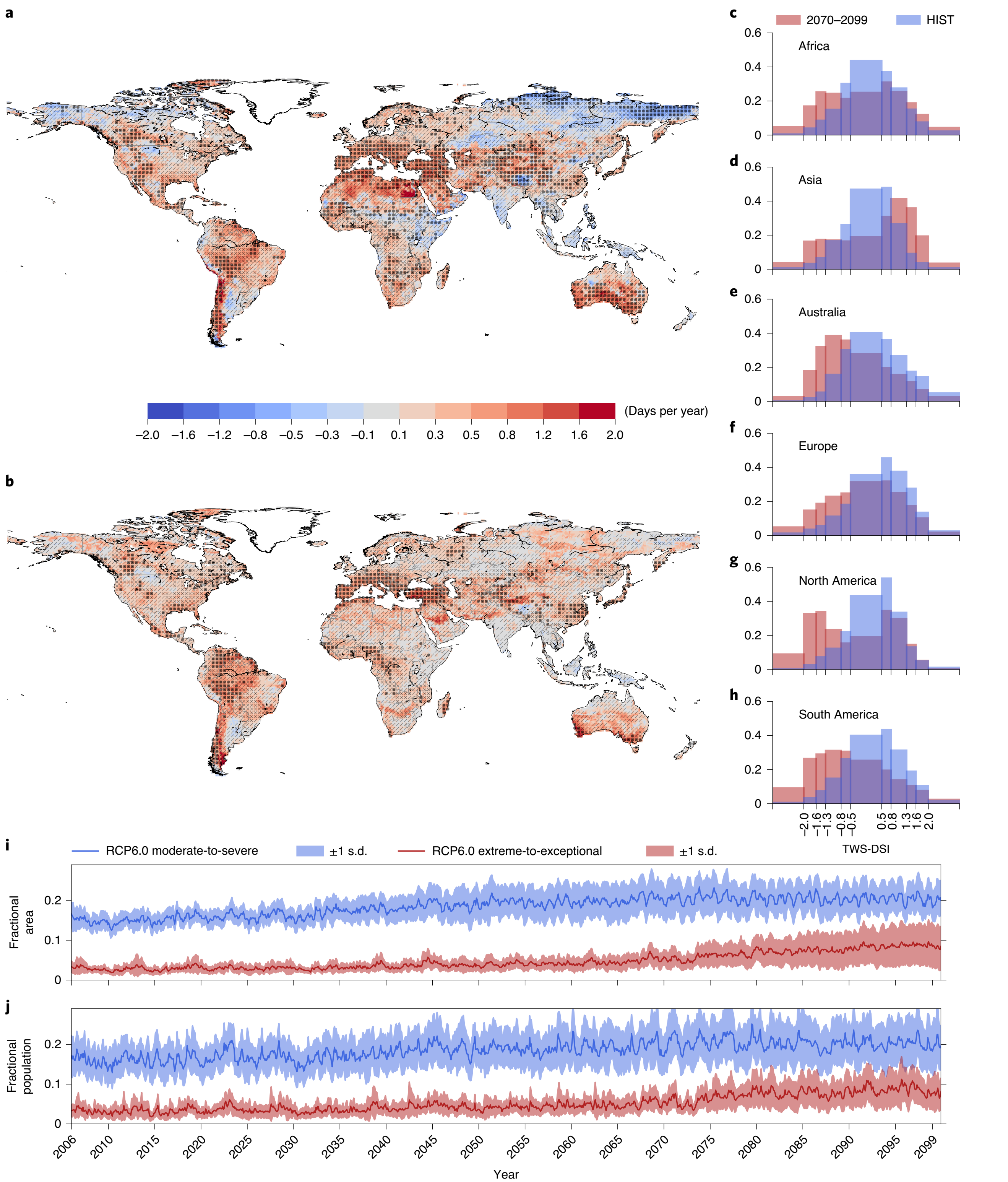

Fig. 4 | Projected changes in occurrence and time evolution of droughts under RCP6.0. a,**b**, Maps showing the trend (days per year) in the frequency of moderate-to-severe (**a**) and extreme-to-exceptional (**b**) droughts for the 2006–2099 period. The single and double hatches show regions where >50% and >75% of the ensemble members, respectively, agree in the sign of change. Stippling marks regions where >50% of ensemble members show a significant trend (Mann–Kendall test at a 5% significance level). **c**–**h**, Histograms showing the frequency of droughts with varying severity indicated by monthly TWS-DSI on the *x* axis (see Methods and Supplementary Tables 1 and 4), averaged over the continents for the baseline period (HIST; 1976–2005) and late twenty-first century (2070–2099). **i**,**j**, The change in the fractional global land area (excluding Greenland and Antarctica) (**i**) and population projections under Shared Socioeconomic Pathway 2 (SSP2; **j**) to experience moderate-to-severe (blue) and extreme-to-exceptional (red) droughts; shaded areas indicate ±1 standard deviation (s.d.) from the ensemble mean, representing the spread in the projection among ensemble members. Results for RCP2.6 are shown in Supplementary Fig. 4.

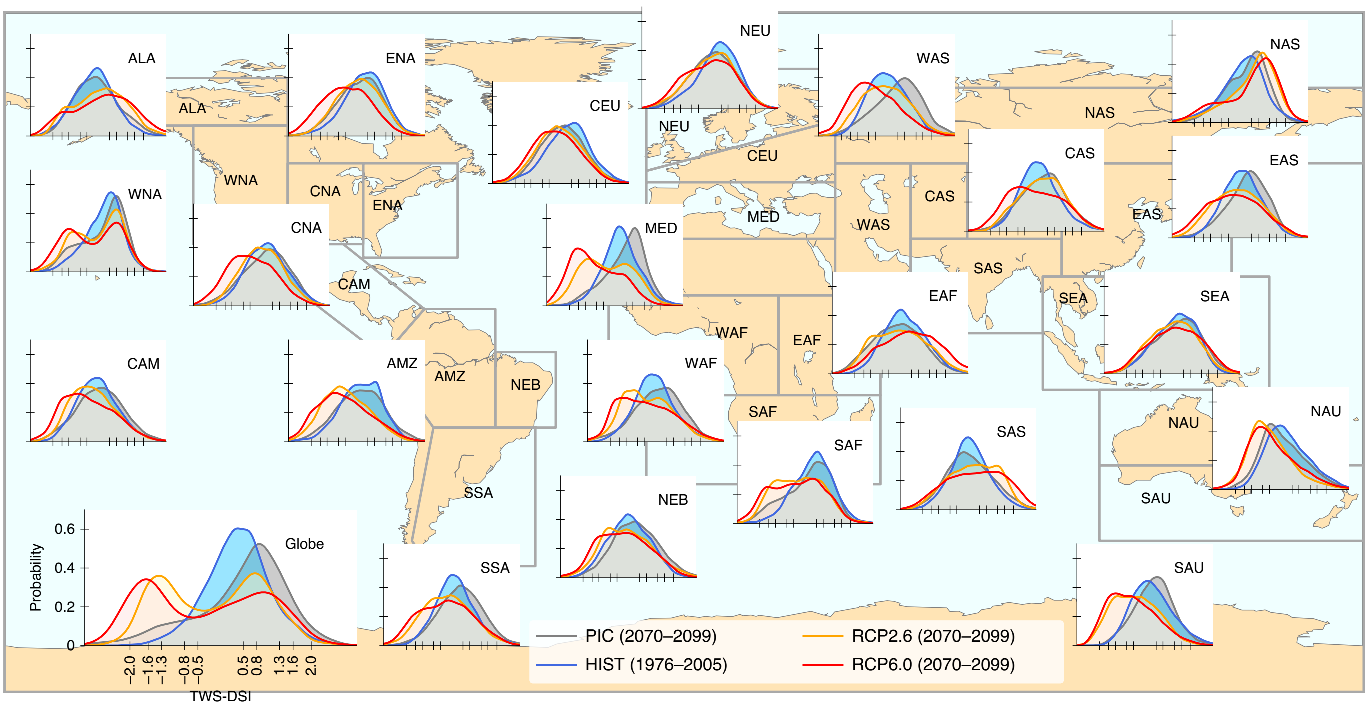

Fig. 5 | PDF of monthly TWS-DSI for the late twenty-first century. Ensemble simulations grouped for different cases (that is, HIST, PIC, RCP2.6 and RCP6.0). The labels are indicated in the inset for the entire globe. A description of the SREX regions (background map) is provided in Supplementary Fig. 3. Similar results for the mid-twenty-first century are shown in Supplementary Fig. 5.

(centred at TWS-DSI = 0) for the historical period tend to become more positively skewed in most regions where TWS is expected to decline (Figs. 1 and 3), meaning that these regions are likely to experience more frequent and intense TWS droughts in the future. For example, in AMZ the occurrence of severe, extreme and exceptional TWS droughts (Supplementary Table 1) increases substantially (under both RCPs) by mid- and late twenty-first century (Fig. 5). The dry-season TWS deficit in the Amazon river basin is suggested to be increasing, causing more frequent and intense droughts[20,44], and our findings highlight that the drying would further intensify, with important implications for the resilience of the Amazonian rainforest.

Distributions with an obvious positive skew for the future periods can be observed in CAM, CNA, MED, NAU, SAU, WAF and WAS. Conversely, regions such as EAF, NAS and SAS are projected to experience a reduced frequency of TWS droughts. For West North America (WNA) and the entire globe, a shift in the PDFs to a bimodal distribution can be seen, suggesting an increased frequency of both TWS droughts and anomalously wet conditions, further indicating a reduced TWS buffer capacity under future climate. Finally, the results indicate that in the absence of greenhouse gas forcing (PIC simulation; Fig. 5), future TWS droughts would have not changed noticeably or their severity could have been reduced in many regions, suggesting that the exacerbations in drought conditions are attributable primarily to climate change.

A comparison of TWS-DSI with traditional drought indices (Methods and Extended Data Figs. 7–10) suggests that TWS-DSI provides new information on future droughts. Unlike SRI that is highly correlated with SPI, TWS-DSI exhibits different PDFs in most SREX regions (Fig. 5 and Extended Data Figs. 7 and 8) because it encompasses all relevant storage components related to drought and accounts for land and water management that directly alters water availability. We find that TWS-DSI also differs from soil moisture-based indices (Fig. 5 and Extended Data Figs. 9 and 10) because the soil moisture contribution to total TWS varies substantially among regions (Extended Data Fig. 6); TWS-DSI captures the effects of groundwater and surface water storages, and accounts for land and water management activities not reflected in the other indices. These comparisons—supported by previous studies on historical droughts[6,36,37]—indicate that TWS-DSI could be used synergistically with traditional drought indices to better understand and predict droughts by accounting for the role of groundwater and human activities.

Summary and implications

These results show that climate change could reduce TWS in many regions, especially in the Southern Hemisphere, the United States and southwestern Europe; exceptions are regions with high increases in precipitation, including east Africa and northern Asia. By the late twenty-first century and under RCP6.0, two-thirds of the global land could experience a reduction in TWS. We find strong agreement among ensemble model projections, especially in the direction of change, suggesting that the results are robust. We further show that TWS extreme droughts are expected to become more frequent in most of the SREX regions. Globally, land area and projected population in extreme-to-exceptional TWS drought under RCP6.0 are projected to more than double, each increasing from 3% to 7% and 8%, respectively, by the late twenty-first century.

While we use state-of-the-art models and the best available global data available, there are limitations to our approach. First, even though the GHMs/LSMs reproduce historical TWS variability well, these models and the GCM forcing data contain inherent biases[9]. Second, assessment of the relative contributions of individual TWS components is limited to soil moisture, because the other components are not currently available from ISIMIP2b simulations. Last, the implications of vegetation response to rising CO_2 levels on TWS and drought projections are not considered, because the hydrological models (except LPJmL) do not currently simulate vegetation dynamics. Studies have shown that elevated atmospheric CO_2 levels lead to increased leaf-level water-use efficiency, potentially ameliorating the reduction in water availability through reduced evapotranspiration and increased soil moisture and runoff[45,46]. This implies that the projected decline in TWS and increase in future droughts may be overestimated in our study. However, increased foliage area under elevated CO_2 levels and warmer climate generally lead to increased vegetation growth and associated water use, resulting in decreased water availability by counterbalancing the increase in runoff from water-use efficiency gains[47,48]. Thus, a comprehensive analysis of TWS projections using coupled hydrological–dynamic vegetation models is required for a robust estimation of the implications of vegetation response to elevated CO_2 levels, which should be a priority for future studies.

Despite some limitations, our study provides a comprehensive assessment of climate impacts on future TWS and related droughts. Given large uncertainties and medium confidence in drought projections using traditional drought indices[49], and as no single drought index can capture the diverse set of drought impacts from climate change[50], our results provide information to better predict future droughts and understand water resource and vegetation growth impacts[6,36,37].

Online content

Any methods, additional references, Nature Research reporting summaries, source data, extended data, supplementary information, acknowledgements, peer review information; details of author contributions and competing interests; and statements of data and code availability are available at https://doi.org/10.1038/s41558-020-00972-w.

Received: 17 December 2019; Accepted: 24 November 2020;
Published online: 11 January 2021

References

1. Rodell, M. et al. Emerging trends in global freshwater availability. *Nature* **557**, 651–659 (2018).
2. Tapley, B. D. et al. Contributions of GRACE to understanding climate change. *Nat. Clim. Change* **9**, 358–369 (2019).
3. Thomas, A. C., Reager, J. T., Famiglietti, J. S. & Rodell, M. A GRACE-based water storage deficit approach for hydrological drought characterization. *Geophys. Res. Lett.* **41**, 1537–1545 (2014).
4. Houborg, R., Rodell, M., Li, B., Reichle, R. & Zaitchik, B. F. Drought indicators based on model-assimilated Gravity Recovery and Climate Experiment (GRACE) terrestrial water storage observations. *Water Resour. Res.* **48**, W07525 (2012).
5. Zhao, M., Velicogna, I. & Kimball, J. S. Satellite observations of regional drought severity in the continental United States using GRACE-based terrestrial water storage changes. *J. Clim.* **30**, 6297–6308 (2017).
6. Long, D. et al. GRACE satellite monitoring of large depletion in water storage in response to the 2011 drought in Texas. *Geophys. Res. Lett.* **40**, 3395–3401 (2013).
7. Reager, J., Thomas, B. & Famiglietti, J. River basin flood potential inferred using GRACE gravity observations at several months lead time. *Nat. Geosci.* **7**, 588–592 (2014).
8. Pokhrel, Y. et al. Model estimates of sea-level change due to anthropogenic impacts on terrestrial water storage. *Nat. Geosci.* **5**, 389–392 (2012).
9. Scanlon, B. R. et al. Global models underestimate large decadal declining and rising water storage trends relative to GRACE satellite data. *Proc. Natl Acad. Sci. USA* **115**, E1080–E1089 (2018).
10. Reager, J. et al. A decade of sea level rise slowed by climate-driven hydrology. *Science* **351**, 699–703 (2016).
11. Wang, J. et al. Recent global decline in endorheic basin water storages. *Nat. Geosci.* **11**, 926–932 (2018).
12. Pokhrel, Y. et al. Incorporation of groundwater pumping in a global Land Surface Model with the representation of human impacts. *Water Resour. Res.* **51**, 78–96 (2015).
13. Wada, Y. et al. Human–water interface in hydrological modelling: current status and future directions. *Hydrol. Earth Syst. Sci.* **21**, 4169–4193 (2017).
14. Döll, P., Müller Schmied, H., Schuh, C., Portmann, F. T. & Eicker, A. Global-scale assessment of groundwater depletion and related groundwater abstractions: combining hydrological modeling with information from well observations and GRACE satellites. *Water Resour. Res.* **50**, 5698–5720 (2014).
15. Hanasaki, N., Yoshikawa, S., Pokhrel, Y. & Kanae, S. A global hydrological simulation to specify the sources of water used by humans. *Hydrol. Earth Syst. Sci.* **22**, 789–817 (2018).
16. Felfelani, F., Wada, Y., Longuevergne, L. & Pokhrel, Y. Natural and human-induced terrestrial water storage change: a global analysis using hydrological models and GRACE. *J. Hydrol.* **553**, 105–118 (2017).
17. Rodell, M., Velicogna, I. & Famiglietti, J. S. Satellite-based estimates of groundwater depletion in India. *Nature* **460**, 999–1002 (2009).
18. Scanlon, B. R. et al. Groundwater depletion and sustainability of irrigation in the US High Plains and Central Valley. *Proc. Natl Acad. Sci. USA* **109**, 9320–9325 (2012).
19. Famiglietti, J. S. et al. Satellites measure recent rates of groundwater depletion in California's Central Valley. *Geophys. Res. Lett.* **38**, L03403 (2011).
20. Chaudhari, S., Pokhrel, Y., Moran, E. & Miguez-Macho, G. Multi-decadal hydrologic change and variability in the Amazon River basin: understanding terrestrial water storage variations and drought characteristics. *Hydrol. Earth Syst. Sci.* **23**, 2841–2862 (2019).
21. Schewe, J. et al. Multimodel assessment of water scarcity under climate change. *Proc. Natl Acad. Sci. USA* **111**, 3245–3250 (2014).
22. Oki, T. & Kanae, S. Global hydrological cycles and world water resources. *Science* **313**, 1068–1072 (2006).
23. Ferguson, C., Pan, M. & Oki, T. The effect of global warming on future water availability: CMIP5 synthesis. *Water Resour. Res.* **54**, 7791–7819 (2018).
24. Pokhrel, Y., Fan, Y. & Miguez-Macho, G. Potential hydrologic changes in the Amazon by the end of the twenty-first century and the groundwater buffer. *Environ. Res. Lett.* https://doi.org/10.1088/1748-9326/9/8/084004 (2014).
25. Jensen, L., Eicker, A., Dobslaw, H., Stacke, T. & Humphrey, V. Long-term wetting and drying trends in land water storage derived from GRACE and CMIP5 models. *J. Geophys. Res. Atmos.* **124**, 9808–9823 (2019).
26. Freedman, F. R., Pitts, K. L. & Bridger, A. F. Evaluation of CMIP climate model hydrological output for the Mississippi River Basin using GRACE satellite observations. *J. Hydrol.* **519**, 3566–3577 (2014).
27. Nasrollahi, N. et al. How well do CMIP5 climate simulations replicate historical trends and patterns of meteorological droughts? *Water Resour. Res.* **51**, 2847–2864 (2015).
28. Mach, K. J. et al. Climate as a risk factor for armed conflict. *Nature* **571**, 193–197 (2019).
29. McKee, T. B., Doesken, N. J. & Kleist, J. The relationship of drought frequency and duration to time scales. In *Proc. 8th Conference on Applied Climatology* 179–183 (1993).
30. Palmer, W. *Meteorological Drought* Research Paper No. 45 (US Weather Bureau, 1965).
31. Samaniego, L., Kumar, R. & Zink, M. Implications of parameter uncertainty on soil moisture drought analysis in Germany. *J. Hydrometeorol.* **14**, 47–68 (2013).
32. Sheffield, J. & Wood, E. F. Projected changes in drought occurrence under future global warming from multi-model, multi-scenario, IPCC AR4 simulations. *Clim. Dyn.* **31**, 79–105 (2008).
33. Shukla, S. & Wood, A. W. Use of a standardized runoff index for characterizing hydrologic drought. *Geophys. Res. Lett.* **35**, L02405 (2008).
34. Dai, A. Increasing drought under global warming in observations and models. *Nat. Clim. Change* **3**, 52–58 (2013).
35. Van Loon, A. F. Hydrological drought explained. *WIREs Water* **2**, 359–392 (2015).
36. Du, J. et al. Multicomponent satellite assessment of drought severity in the contiguous United States from 2002 to 2017 using AMSR-E and AMSR2. *Water Resour. Res.* **55**, 5394–5412 (2019).
37. Geruo, A. et al. Satellite-observed changes in vegetation sensitivities to surface soil moisture and total water storage variations since the 2011 Texas drought. *Environ. Res. Lett.* **12**, 054006 (2017).
38. Frieler, K. et al. Assessing the impacts of 1.5°C global warming – simulation protocol of the Inter-Sectoral Impact Model Intercomparison Project (ISIMIP2b). *Geosci. Model Dev.* **10**, 4321–4345 (2017).
39. Sanderson, B. M., Wehner, M. & Knutti, R. Skill and independence weighting for multi-model assessments. *Geosci. Model Dev.* **10**, 2379–2395 (2017).
40. Gudmundsson, L., Seneviratne, S. I. & Zhang, X. Anthropogenic Climate Change detected in European renewable freshwater resources. *Nat. Clim. Change* **7**, 813–816 (2017).
41. Boisier, J. P., Ciais, P., Ducharne, A. & Guimberteau, M. Projected strengthening of Amazonian dry season by constrained climate model simulations. *Nat. Clim. Change* **5**, 656–660 (2015).
42. Malhi, Y. et al. Climate change, deforestation, and the fate of the Amazon. *Science* **319**, 169–172 (2008).
43. Getirana, A., Kumar, S., Girotto, M. & Rodell, M. Rivers and floodplains as key components of global terrestrial water storage variability. *Geophys. Res. Lett.* **44**, 10359–10368 (2017).

44. Jiménez-Muñoz, J. C. et al. Record-breaking warming and extreme drought in the Amazon rainforest during the course of El Niño 2015–2016. *Sci. Rep.* **6**, 33130 (2016).
45. Berg, A. et al. Land–atmosphere feedbacks amplify aridity increase over land under global warming. *Nat. Clim. Change* **6**, 869–874 (2016).
46. Lemordant, L., Gentine, P., Swann, A. S., Cook, B. I. & Scheff, J. Critical impact of vegetation physiology on the continental hydrologic cycle in response to increasing CO_2. *Proc. Natl Acad. Sci. USA* **115**, 4093–4098 (2018).
47. Mankin, J. S., Seager, R., Smerdon, J. E., Cook, B. I. & Williams, A. P. Mid-latitude freshwater availability reduced by projected vegetation responses to climate change. *Nat. Geosci.* **12**, 983–988 (2019).
48. Singh, A., Kumar, S., Akula, S., Lawrence, D. M. & Lombardozzi, D. L. Plant growth nullifies the effect of increased water-use efficiency on streamflow under elevated CO_2 in the Southeastern United States. *Geophys. Res. Lett.* **47**, e2019GL086940 (2020).
49. Seneviratne, S. I. et al. in *Managing the Risks of Extreme Events and Disasters to Advance Climate Change Adaptation* (ed. C. B. Field) 109–230 (Cambridge Univ. Press, 2017).
50. Wanders, N., Loon, A. F. V. & Van Lanen, H. A. Frequently used drought indices reflect different drought conditions on global scale. *Hydrol. Earth Syst. Sci. Discuss.* (in the press).

Methods

Models, simulation settings and forcing data. The seven terrestrial hydrology models used in this study include five GHMs[51]: CWatM[52], H08[15,53,54], MPI-HM[55], PCR-GLOBWB[56] and WaterGAP2[57]; one global LSM[51]: CLM4.5[58]; and one dynamic global vegetation model: LPJmL[59]. All models simulate the key terrestrial hydrological (for example, soil, vegetation and river) processes (Supplementary Table 3). Meteorological forcing data are derived from climate simulations by four of the GCMs (a subset of models participating in the Coupled Model Intercomparison Project Phase 5) included in the Fifth Assessment Report of the IPCC: GFDL-ESM2M, HadGEM2-ES, IPSL-CM5A-LR and MIROC5. The climate variables included in the forcing data are precipitation, air temperature, solar radiation (short and long wave), wind speed, specific humidity and surface pressure, which are bias adjusted[60] and downscaled to 0.5°×0.5° spatial resolution of the terrestrial hydrology models. A comprehensive description of bias adjustment and downscaling can be found in the previous literature[60–62].

For each GCM, four radiative forcing cases are considered for varying periods (Supplementary Table 2): the pre-industrial control (PIC; pre-industrial climate; 1861–2099), historical climate (HIST; which includes the effects of human emissions including greenhouse gases and aerosols[63]; 1861–2005), a low greenhouse gas concentration scenario (RCP2.6; 2006–2099) and a medium–high greenhouse gas concentration scenario (RCP6.0; 2006–2099). Simulations are conducted under the standard protocol of the Group-2 simulation scenario design of ISIMIP2b[38] (https://www.isimip.org/). The two RCPs are the only RCPs for which TWS results from all models were available from ISIMIP2b simulations. The hydrology models are run for each GCM–radiative forcing combination by considering time-varying land and water management activities and socioeconomic conditions for the HIST runs but fixed at the present day (that is, 2005) level for future projections (2006–2099; RCP2.6 and RCP6.0). For the PIC simulations, climate forcing is set at the pre-industrial level and land and water management activities and socioeconomic conditions vary for the historical period but are fixed at 2005 level for the future periods (see Fig. 1 in Frieler et al.[38]). Thus, while the difference between PIC and other radiative forcing cases results from pure climate change, the difference between historical and future PIC runs reflects the time-varying effects of human activities and socioeconomic drivers, not climate change. The human activities and socioeconomic indicators considered are population, national gross domestic product, land-use and land-cover change, irrigated areas, fertilizer use and reservoir operation including water withdrawal, depending on the model schemes. Land-use and land-cover change and irrigated areas are prescribed on the basis of the HYDE3–MIRCA data[64–66] and data for dams and reservoirs are taken from the GRanD database[67]. Irrigation (and other water-use sector) schemes vary among models (Supplementary Table 3) but all models simulate global irrigation requirements within plausible limits of reported datasets based on country statistics (see the reference to each model for more details). The reservoir operation schemes are based on Hanasaki et al.[68] (H08 and WaterGAP2), Biemans et al.[69] (LPJmL) and a combination of Haddeland et al.[70] and Adams et al.[71] (CWatM and PCR-GLOBWB); reservoirs are not represented in MPI-HM and CLM4.5. Soil column depth and layer configuration and groundwater representation vary among models (Supplementary Table 3).

Multi-model weighted mean. The multi-model mean is calculated by weighting the ensemble members on the basis of their skill (that is, the root mean squared error (RMSE) of the area-weighted seasonal cycle of TWS relative to GRACE data) and independence (that is, a measure of how different model results are) scores, following previous studies[39,72]. The continent-based, temporally static weights ($w_o(i)$) for the 27 ensemble members (Extended Data Fig. 1) are calculated as the normalized product of the skill and independence weights so that their sum is unity[39,72]; that is, $\left(\sum_{i=1}^{27} w_o(i) = 1\right)$. The independence weight of member i, $w_u(i)$, is computed as the inverse of the summation of the pairwise similarity score, $S(\delta_{i,j})$, which ranges between 1 (for identical members) and 0 (for the most distinct members). Mathematically, $w_u(i) = \frac{1}{1+\sum_{j\neq i}^{27} S(\delta_{i,j})}$. The pairwise similarity score is calculated as a function of the Euclidean distance[39] between the members ($\delta_{i,j}$), represented by the RMSE of the continent-level average TWS seasonal cycle from two members, and a parameter called the radius of similarity (D_u): $S(\delta_{i,j}) = \exp\left(-\left(\frac{\delta_{i,j}}{D_u}\right)^2\right)$, where $\delta_{i,j}$ is normalized by the mean of pairwise inter-model distances (Extended Data Fig. 2). The parameter D_u is the distance below which models are marked as similar and is resolved for each continent as a fraction of the distance between the best performing member (that is, the model with the smallest RMSE) and GRACE through an iterative process[39]. The skill weighting of member i, $w_q(i)$, is calculated on the basis of the stretched exponential function[73] of the distance from GRACE ($\delta_{i,\mathrm{GRACE}}$; the normalized RMSE of member i's TWS seasonal cycle against GRACE for 2002–2016) and the radius of model quality (D_q) : $w_q(i) = \exp\left(-\left(\frac{\delta_{i,\mathrm{GRACE}}}{D_q}\right)^2\right)$, where smaller distances from the GRACE seasonal cycle result in larger skill scores/weights. The parameter D_q is also defined as a fraction of the distance between the best performing member and GRACE. This parameter controls the strength of the skill weighting. That is, when D_q approaches zero, most of the simulations get largely down-weighted and only the best performing model is assigned a high skill score. Conversely, as D_q approaches infinity, all ensemble members are allotted a high (that is, close to 1) skill score alike, and therefore, the multi-model weighted mean approaches the non-skilled weighted mean. Finally, the continent-based D_q values are estimated for the 2002–2016 period and tested for RCP6.0 late century simulations following a perfect model test and through an iterative procedure[39]. The perfect model test is conducted to ensure that out-of-sample simulations (that is, simulations out of the GRACE period) are also improved with the weighting scheme. Note that the model weights are estimated by using the seasonal cycle of TWS, rather than the trend or interannual variability, because the original study[39] that described the weighing scheme used the seasonality of climate variables, and no studies have demonstrated the applicability or robustness of the schemes based on trend or interannual variability. Further, the GRACE data period is relatively short to rely on temporal trends, which are highly sensitive to the time window chosen.

Simulated TWS, GRACE data, model evaluation and TWS variability under climate change. The monthly scale simulated TWS is derived by vertically integrating the surface and subsurface water storages, which include snow, canopy, river, reservoir (if simulated), lake (if simulated), wetland (if simulated), soil and groundwater storages[74,75]. TWS derived from GRACE satellite measurements is used to evaluate the simulated TWS for the 2002–2016 period. We use the mean of mascon products[76] from two processing centres: the Center for Space Research at the University of Texas at Austin, and the Jet Propulsion Laboratory at the California Institute of Technology. For model results, as the evaluation period is not covered completely by HIST simulations, we combine the results from HIST simulations (2002–2005) with results from RCP2.6 (2006–2016). The seasonal mean of TWS anomalies (Extended Data Fig. 5 and Supplementary Fig. 1) is derived by first calculating the climatological mean seasonal cycle of TWS for the evaluation period and then taking the mean for each season. For consistency, the same reference period (2002–2016) is used in calculating the seasonal anomalies for both GRACE data and model simulations. Changes in TWS for the mid- (2030–2059) and late (2070–2099) twenty-first century (for the two RCPs) are calculated by taking the difference of the mean TWS for those periods to the mean TWS for the historical baseline period of 1976–2005, which is the last 30-year period of the historical simulations; simulations from the year 2006 are conducted under future climate scenarios.

Quantification of uncertainty in TWS simulations. The contribution of uncertainties from GCMs (that is, forcing data) and GHMs/LSMs to TWS is quantified by using the sequential sampling approach[77]. In this approach, the uncertainty contribution of GCMs and GHMs/LSMs is calculated using the range statistic[77] of monthly TWS (represented as the quantile-based TWS index) averaged over the SREX regions for the historical baseline period, and mid- and late twenty-first century. The GCMs (GHMs/LSMs) uncertainty—characterized as the range of the mean in the quantile-based TWS index—for a given RCP scenario is computed by first averaging the quantile-based TWS index across all GHMs/LSMs (GCM) for each of the GCMs (GHMs/LSMs) and then calculating the range across GCMs (GHMs/LSMs). The quantile-based TWS index, spatially averaged over SREX regions, is calculated[31] by fitting a non-parametric kernel density function to TWS data, estimating the PDF and numerically integrating the PDF between zero and the simulated TWS.

Component contribution of soil moisture to total TWS. A dimensionless metric, CCR[16,78], is used to quantify the contribution of soil moisture to total TWS (Extended Data Fig. 6). CCR represents the ratio of the seasonal amplitude of soil moisture to that of TWS. The CCR is used to assess the differences between the drought projected by the TWS-DSI and SMI. The contribution of other TWS components could not be examined as those variables are not currently available from ISIMIP2b simulations.

TWS-DSI and drought severity under climate change. Monthly TWS-DSI is estimated for all ensemble members following Zhao et al.[5]; $\text{TWS-DSI}_{i,j} = (\text{TWS}_{i,j} - \mu_j)/\sigma_j$, where $\text{TWS}_{i,j}$ is the TWS anomaly in year i and month j, and μ_j and σ_j are the climatological mean and standard deviation, respectively, of monthly TWS anomalies for the reference period. $\text{TWS-DSI}_{i,j}$ is a non-dimensional index that defines droughts with varying degrees of severity, also representing wet conditions (Supplementary Table 1). In calculating the mean and standard deviation of TWS for any specified period, a common reference period set to 1861–2099 is used to avoid potential exaggeration in the estimates of TWS variability and drought evolution[79], and for consistent comparison. The drought trend (Fig. 4a,b) is calculated as the linear least-squares trend using the time series of annual drought occurrence presented in days per year. The significance of trend values is evaluated using the non-parametric Mann–Kendall trend test[80,81] with a 5% significance level. Note that for the trend calculations, four drought types are re-grouped into two major categories for simplicity: moderate-to-severe ($-1.6 < \text{TWS-DSI} \leq -0.8$) and extreme-to-exceptional ($\text{TWS-DSI} \leq -1.6$) droughts (see Supplementary Table 1 for more details).

The frequency of droughts with varying severities used for continental-scale drought analysis (Fig. 4c–h) is estimated by considering the TWS-DSI calculated for all ensemble members, normalized such that the results show the PDF at bins corresponding to the classes of drought and wet conditions (Supplementary Table 1). For the analysis of the global population affected by drought, we use the time-varying (2006–2100) gridded global population data generated by scaling the 2005 population data from the Center for International Earth Science Information Network at Columbia University (https://sedac.ciesin.columbia.edu/) with the country-level future population growth rate (https://tntcat.iiasa.ac.at/SspDb) for SSP2 (ref. [82]) Among the five SSPs, SSP2 reflects an intermediate, middle-of-the-road scenario in which population growth is medium[83]. The changes in future population under drought are estimated relative to the baseline period of 1976–2005 but using static population data for 2005. Finally, the PDFs for each IPCC SREX region (Fig. 5) are estimated using the non-parametric kernel density method[84] and by considering all ensemble members. There is a bimodality in the PDF of TWS-DSI in some regions as a result of preferential states in water stores such as soil moisture[85,86], thus using the non-parametric kernel density method is more appropriate compared to the parametric unimodal distributions with underlying assumptions such as normality[27,31]. We find that using the kernel density method to estimate the PDF of TWS-DSI results in almost identical PDF estimation (not shown) to that from the conventional standardized drought indices[29]—that is, by first fitting the TWS data to a secondary distribution (for example, gamma, Pearson type III) and then transforming it to a standard normal distribution.

The SPI[29] and SRI[33] (Extended Data Figs. 7 and 8) are calculated by first fitting the monthly precipitation and runoff data, respectively, to the gamma distribution function to obtain monthly climatological distributions for the reference period (1861–2099). These distributions are then used to estimate the cumulative probability of the variable (precipitation or runoff) for a certain period. Finally, the cumulative probabilities are converted to standard normal deviates ($\mu = 0$ and $\sigma = 1$) by inversing the respective cumulative distribution function. The SMI is estimated on the basis of two approaches. For the direct comparison with TWS-DSI, SMI is obtained using the same methodology as TWS-DSI[5], however using soil moisture data instead of TWS (Extended Data Fig. 9). Additionally, a more conventional quantile-based SMI (Extended Data Fig. 10) is calculated following Samaniego et al.[31] and Sheffield and Wood[32]. To do so, soil moisture is first fitted to a non-parametric kernel density function to derive the monthly climatological PDFs for the reference period (1861–2099). The quantile-based drought index corresponding to a given soil moisture for month i (x_i) is then derived by numerically integrating the respective PDF[31] $\left(\hat{f}\right)$ as: $\mathrm{SMI}_i = \int_0^{x_i} \hat{f}(u)du$. The PDFs of the drought indices (SPI, SRI and SMI) are generated for different periods using the kernel density method (Extended Data Figs. 7–10).

Data availability

The model results are freely available from the ISIMIP project portal (https://www.isimip.org/outputdata/) and the two GRACE products used for model evaluation can be obtained from http://www2.csr.utexas.edu/grace/ and https://podaac.jpl.nasa.gov/GRACE. The processed data used to generate the figures in the main text are available on CUAHSI HydroShare and Figshare (https://doi.org/10.6084/m9.figshare.13218710).

Code availability

All figures were produced using the freely available visualization libraries in Python 3.5 (such as Matplotlib), and statistical analysis was performed using built-in functions in Python 3.5. The relevant portions of the computer code used to process the results and develop the figures are available at https://doi.org/10.5281/zenodo.4266999.

References

51. Haddeland, I. et al. Multimodel estimate of the global terrestrial water balance: setup and first results. *J. Hydrometeorol.* **12**, 869–884 (2011).
52. Burek, P. et al. Development of the Community Water Model (CWatM v1.04) – a high-resolution hydrological model for global and regional assessment of integrated water resources management. *Geosci. Model Dev. Discuss.* **13**, 3267–3298 (2019).
53. Hanasaki, N. et al. An integrated model for the assessment of global water resources – Part 1: model description and input meteorological forcing. *Hydrol. Earth Syst. Sci.* **12**, 1007–1025 (2008).
54. Hanasaki, N. et al. An integrated model for the assessment of global water resources – Part 2: applications and assessments. *Hydrol. Earth Syst. Sci.* **12**, 1027–1037 (2008).
55. Stacke, T. & Hagemann, S. Development and evaluation of a global dynamical wetlands extent scheme. *Hydrol. Earth Syst. Sci.* **16**, 2915–2933 (2012).
56. Wada, Y., Wisser, D. & Bierkens, M. F. P. Global modeling of withdrawal, allocation and consumptive use of surface water and groundwater resources. *Earth Syst. Dynam.* **5**, 15–40 (2014).
57. Müller Schmied, H. et al. Variations of global and continental water balance components as impacted by climate forcing uncertainty and human water use. *Hydrol. Earth Syst. Sci.* **20**, 2877–2898 (2016).
58. Oleson, K. W. *Technical Description of Version 4.5 of the Community Land Model (CLM)* (National Center for Atmospheric Research, 2013).
59. Bondeau, A. et al. Modelling the role of agriculture for the 20th century global terrestrial carbon balance. *Glob. Change Biol.* **13**, 679–706 (2007).
60. Lange, S. Trend-preserving bias adjustment and statistical downscaling with ISIMIP3BASD (v1. 0). *Geosci. Model Dev.* **12**, 3055–3070 (2019).
61. Hempel, S., Frieler, K., Warszawski, L., Schewe, J. & Piontek, F. A trend-preserving bias correction–the ISI-MIP approach. *Earth Syst. Dyn.* **4**, 219–236 (2013).
62. Lange, S. Bias correction of surface downwelling longwave and shortwave radiation for the EWEMBI dataset. *Earth Syst. Dyn.* **9**, 627–645 (2018).
63. Taylor, K. E., Stouffer, R. J. & Meehl, G. A. An overview of CMIP5 and the experiment design. *Bull. Am. Meteor. Soc.* **93**, 485–498 (2012).
64. Klein Goldewijk, K., Beusen, A., van Drecht, G. & de Vos, M. The HYDE 3.1 spatially explicit database of human-induced global land-use change over the past 12,000 years. *Glob. Ecol. Biogeogr.* **20**, 73–86 (2011).
65. Portmann, F. T., Siebert, S. & Döll, P. MIRCA2000—global monthly irrigated and rainfed crop areas around the year 2000: a new high-resolution data set for agricultural and hydrological modeling. *Glob. Biogeochem. Cycles* **24**, GB1011 (2010).
66. Ramankutty, N., Evan, A. T., Monfreda, C. & Foley, J. A. Farming the planet: 1. Geographic distribution of global agricultural lands in the year 2000. *Glob. Biogeochem. Cycles* **22**, GB1003 (2008).
67. Lehner, B. et al. High-resolution mapping of the world's reservoirs and dams for sustainable river-flow management. *Front. Ecol. Environ.* **9**, 494–502 (2011).
68. Hanasaki, N., Kanae, S. & Oki, T. A reservoir operation scheme for global river routing models. *J. Hydrol.* **327**, 22–41 (2006).
69. Biemans, H. et al. Impact of reservoirs on river discharge and irrigation water supply during the 20th century. *Water Resour. Res.* **47**, W03509 (2011).
70. Haddeland, I., Skaugen, T. & Lettenmaier, D. P. Anthropogenic impacts on continental surface water fluxes. *Geophys. Res. Lett.* **33**, L08406 (2006).
71. Adam, J. C., Haddeland, I., Su, F. & Lettenmaier, D. P. Simulation of reservoir influences on annual and seasonal streamflow changes for the Lena, Yenisei, and Ob' rivers. *J. Geophys. Res. Atmos.* **112**, D24114 (2007).
72. Eyring, V. et al. Taking climate model evaluation to the next level. *Nat. Clim. Change* **9**, 102–110 (2019).
73. Wuttke, J. Laplace–Fourier transform of the stretched exponential function: analytic error bounds, double exponential transform, and open-source implementation "libkww". *Algorithms* **5**, 604–628 (2012).
74. Pokhrel, Y., Fan, Y., Miguez-Macho, G., Yeh, P. J. F. & Han, S.-C. The role of groundwater in the Amazon water cycle: 3. Influence on terrestrial water storage computations and comparison with GRACE. *J. Geophys. Res. Atmos.* **118**, 3233–3244 (2013).
75. Hirschi, M., Seneviratne, S. I. & Schär, C. Seasonal variations in terrestrial water storage for major midlatitude river basins. *J. Hydrometeorol.* **7**, 39–60 (2006).
76. Scanlon, B. R. et al. Global evaluation of new GRACE mascon products for hydrologic applications. *Water Resour. Res.* **52**, 9412–9429 (2016).
77. Samaniego, L. et al. Propagation of forcing and model uncertainties on to hydrological drought characteristics in a multi-model century-long experiment in large river basins. *Climatic Change* **141**, 435–449 (2017).
78. Kim, H., Yeh, P. J. F., Oki, T. & Kanae, S. Role of rivers in the seasonal variations of terrestrial water storage over global basins. *Geophys. Res. Lett.* **36**, L17402 (2009).
79. Sippel, S. et al. Quantifying changes in climate variability and extremes: pitfalls and their overcoming. *Geophys. Res. Lett.* **42**, 9990–9998 (2015).
80. Mann, H. B. Nonparametric tests against trend. *Econometrica* **13**, 245–259 (1945).
81. Kendall, M. *Rank Correlation Measures* 4th edn, Vol. 202 (Charles Griffin, 1975).
82. Riahi, K. et al. The shared socioeconomic pathways and their energy, land use, and greenhouse gas emissions implications: an overview. *Glob. Environ. Change* **42**, 153–168 (2017).
83. Knorr, W., Arneth, A. & Jiang, L. Demographic controls of future global fire risk. *Nat. Clim. Change* **6**, 781–785 (2016).
84. Gatrell, A. C., Bailey, T. C., Diggle, P. J. & Rowlingson, B. S. Spatial point pattern analysis and its application in geographical epidemiology. *Trans. Inst. Br. Geogr.* **21**, 256–274 (1996).
85. D'Odorico, P. & Porporato, A. Preferential states in soil moisture and climate dynamics. *Proc. Natl Acad. Sci. USA* **101**, 8848–8851 (2004).
86. Laio, F., Porporato, A., Ridolfi, L. & Rodriguez-Iturbe, I. On the seasonal dynamics of mean soil moisture. *J. Geophys. Res. Atmos.* **107**, 4272 (2002).

Acknowledgements

Y.P. and F.F. acknowledge support from the National Science Foundation (CAREER Award, grant no. 1752729). H.M.S. and C.-E.T. acknowledge support from the German Federal Ministry of Education and Research (BMBF, grant no. 01LS1711F). J.L. acknowledges support from the Strategic Priority Research Program of Chinese Academy of Sciences (grant no. XDA20060402) and the National Natural Science Foundation of

China (41625001 and 51711520317). N.H. acknowledges support from the ERTDF (2RF-1802) of the ERCA, Japan. Y.W. is supported by the European Union under the Horizon 2020 EUCP project (grant no. 776613) and the JPI Climate and European Union under the ISIpedia project (grant no. 690462). W.T. acknowledges support from the Uniscientia Foundation and the ETH Zurich Foundation (Fel-45 15-1). H.K. acknowledges the Integrated Research Program for Advancing Climate Models (TOUGOU) JPMXD0717935457 from MEXT and the Grantin-Aid for Specially promoted Research 16H06291 from JSPS, Japan.

Author contributions

Y.P. conceived the research. F.F. processed model results, conducted the analyses and prepared graphics. Y.P. and F.F. interpreted the results, and all authors discussed and commented on the outcome. Y.P. prepared the draft with contributions from F.F., and all authors commented on and edited the manuscript.

Competing interests

The authors declare no competing interests.

Additional information

Extended data is available for this paper at https://doi.org/10.1038/s41558-020-00972-w.

Supplementary information is available for this paper at https://doi.org/10.1038/s41558-020-00972-w.

Correspondence and requests for materials should be addressed to Y.P.

Peer review information *Nature Climate Change* thanks Craig Ferguson, Tara Troy and the other, anonymous, reviewer(s) for their contribution to the peer review of this work.

Reprints and permissions information is available at www.nature.com/reprints.

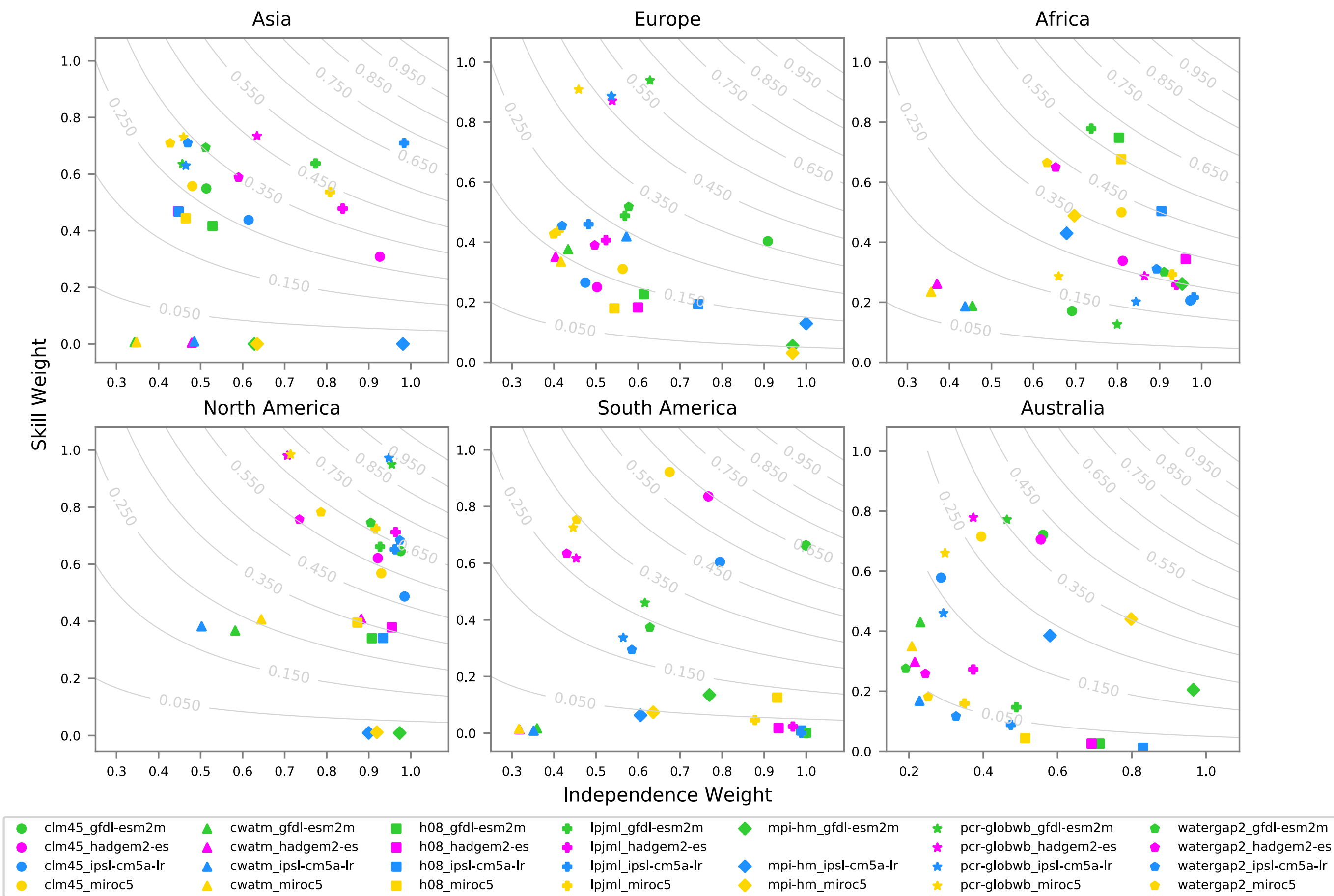

Extended Data Fig. 1 | Continent-based model skill and independence weights (see Methods for details) for 27 ensemble members. The weights are temporally static.

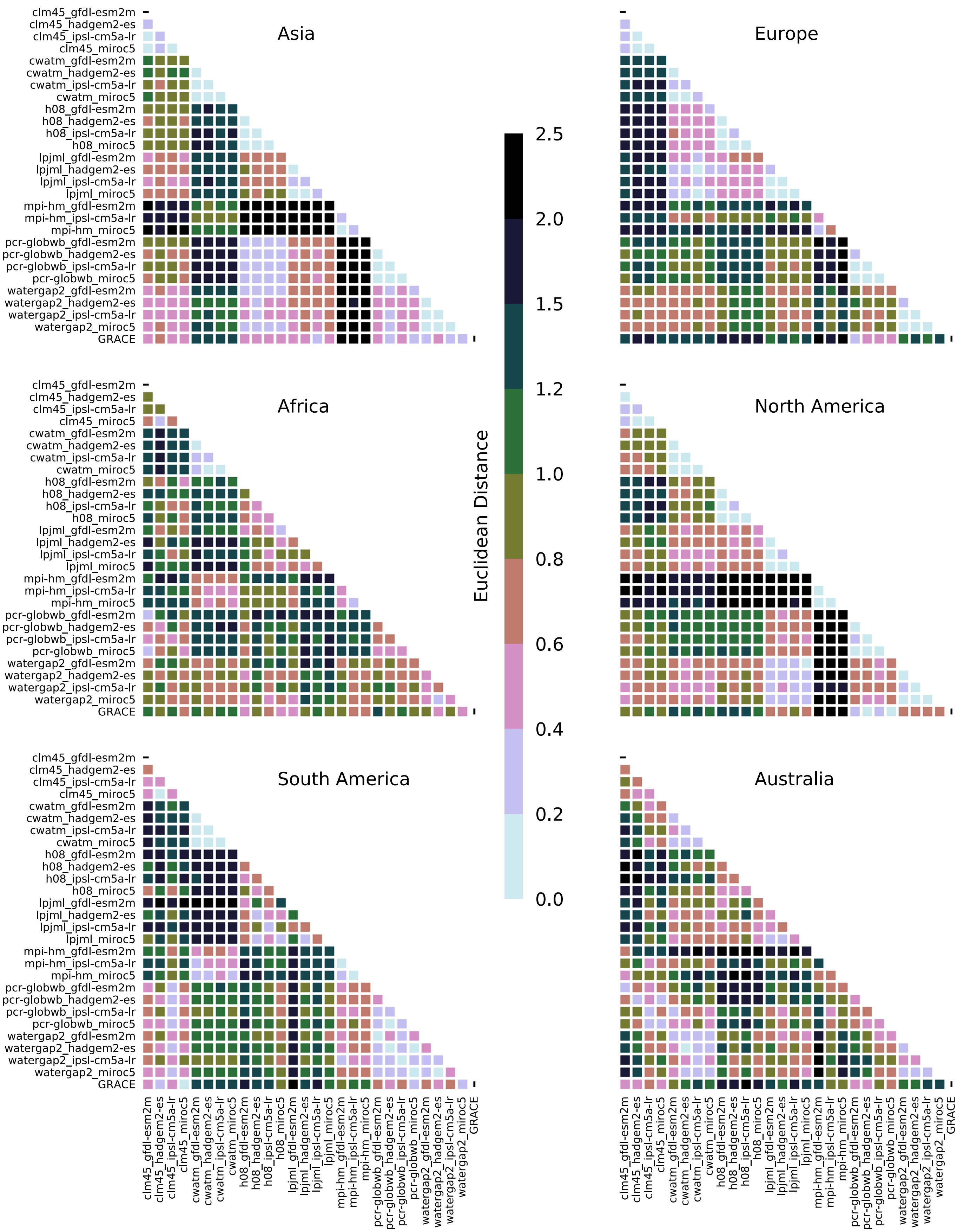

Extended Data Fig. 2 | See next page for caption.

Extended Data Fig. 2 | Continent-based pairwise inter-model distance matrix for ensemble simulations and GRACE observations. Each row or column associates with a single ensemble member or GRACE observations, and each cell represents a pairwise distance of that member compared to the others. Distances are evaluated based on the root mean squared error (RMSE) of TWS seasonal cycle (calculated for 2002–2016 period by combining the results from HIST simulations with RCP2.6), spatially averaged over each continent. The distance for each member is normalized by the mean of pair-wise distances for all members. Lower values of the pairwise distance between two members indicate a better agreement between the two members, and vice versa.

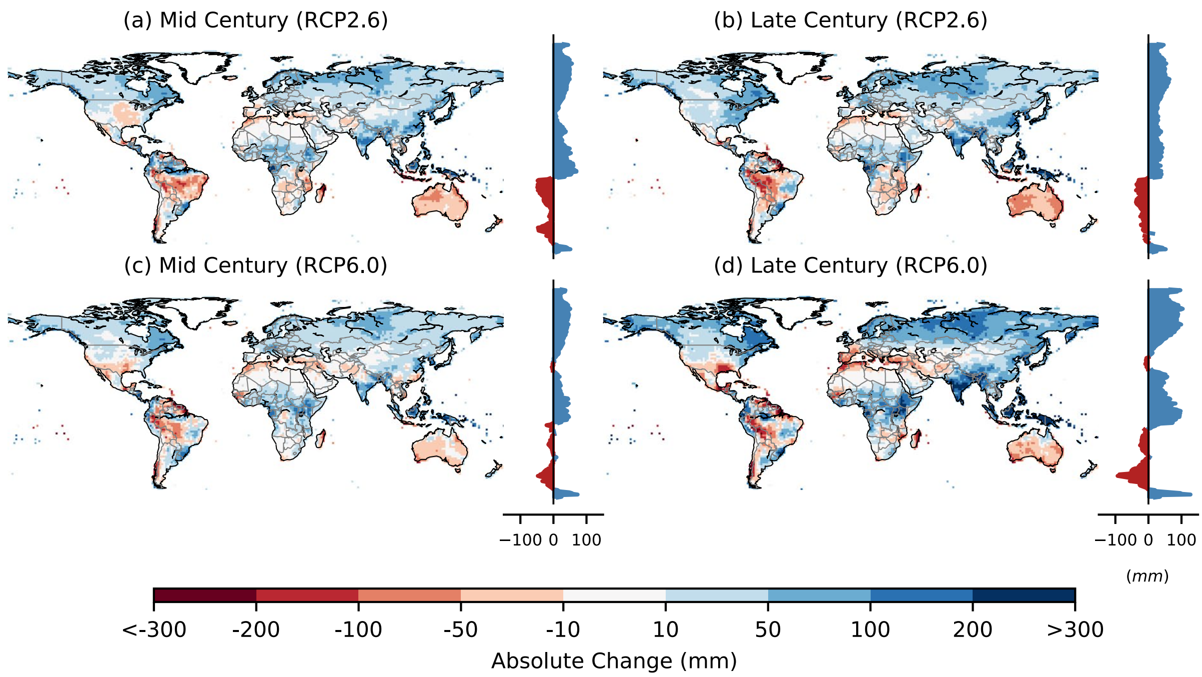

Extended Data Fig. 3 | Spatial patterns of change in precipitation by the mid- (2030–2059) and late- (2070–2099) twenty-first century under RCP 2.6 and 6.0. Shown are the absolute differences in the 30-year mean (mm/year) between the two future periods and historical baseline period of 1976–2005, calculated as the mean of the results from four Global Climate Models (GCMs) used to drive the hydrological models: HadGEM2-ES, GFDL-ESM2M, IPSL-CM5A-LR, and MIROC5. Note that Greenland is masked out. The graph on the right of each panel shows the latitudinal mean.

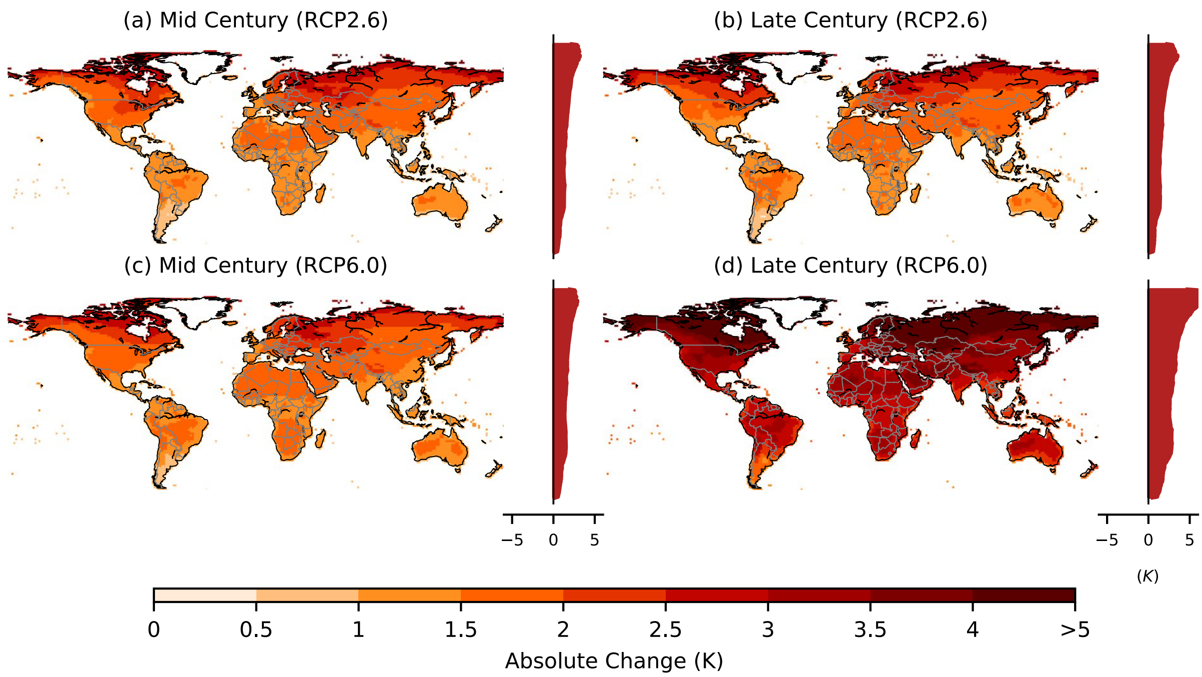

Extended Data Fig. 4 | Spatial patterns of change in air temperature by the mid- (2030–2059) and late- (2070–2099) twenty-first century under RCP 2.6 and 6.0. Shown are the differences in the 30-year mean (Kelvin) between the two future periods and historical baseline period of 1976–2005, calculated as the mean of the results from four GCMs used to drive the hydrological models: HadGEM2-ES, GFDL-ESM2M, IPSL-CM5A-LR, and MIROC5. Note that Greenland is masked out. The graph on the right of each panel shows the latitudinal mean.

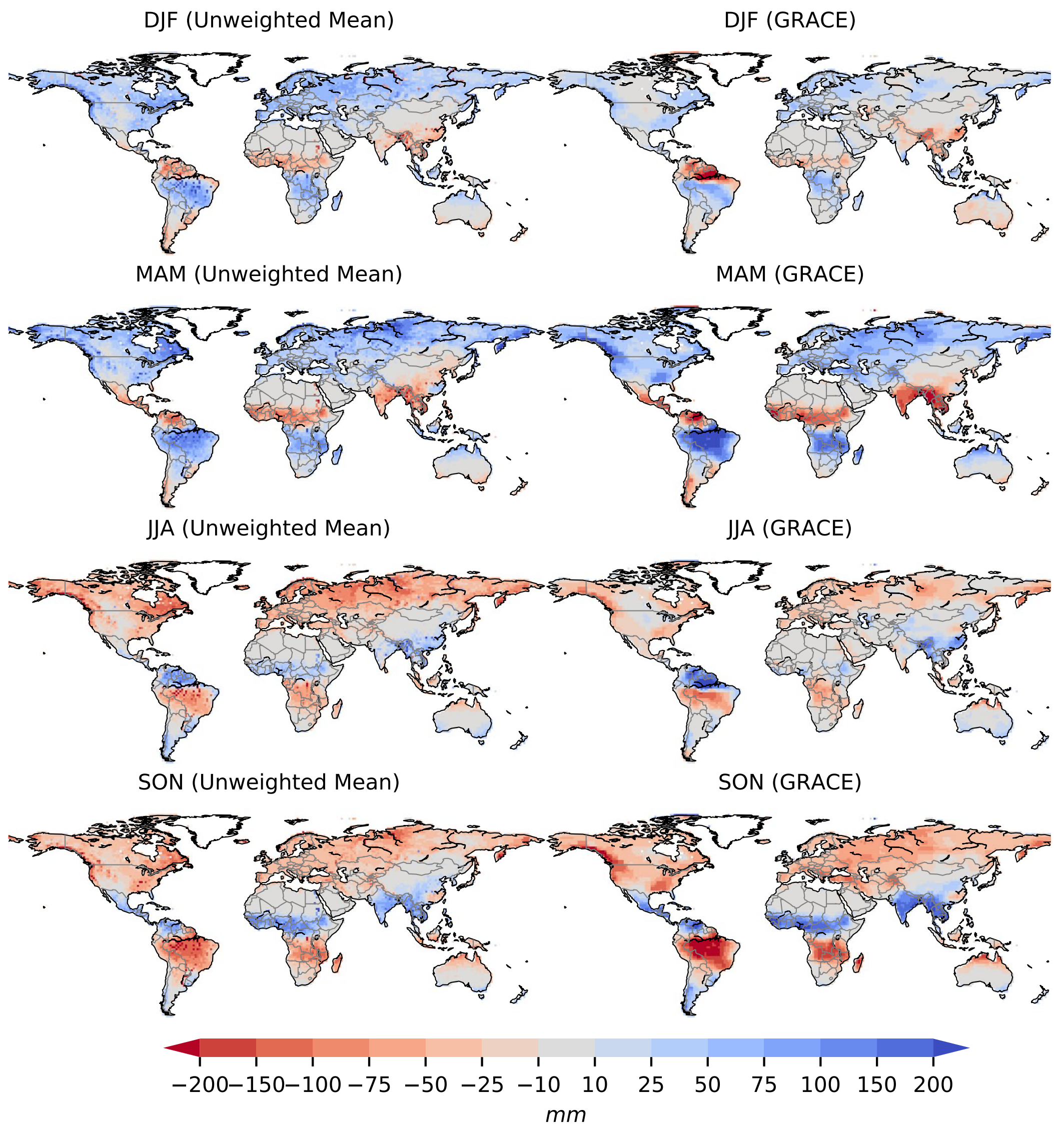

Extended Data Fig. 5 | Spatial patterns of seasonal TWS anomalies from models and GRACE data. Shown are the seasonal averages (December-February (DJF), March-May (MAM), June-August (JJA), and September-November (SON)) of the simulated (multi-model ensemble mean) and GRACE-based monthly TWS deviation from the mean for the GRACE period (2002–2016). Model results for the 2002–2005 period are taken from the historical simulations (see Supplementary Table 2), and for 2006–2016 from RCP2.6 runs (2005soc). Anomalies are calculated by using the mean for 2002–2016 period for both model results and GRACE data. Note that we use the simple ensemble average (not the weighted mean) for these comparisons to provide an unbiased evaluation of the models and to ensure that the model-GRACE agreement is not a result of the weighting that is based on the GRACE data. The results from RCP6.0 (not shown) are almost identical to that shown here. GRACE data shown are the mean of mascon products[76] from two processing centers: the Center for Space Research (CSR) at the University of Texas at Austin (http://www2.csr.utexas.edu/grace/) and NASA Jet Propulsion Laboratory (JPL; https://podaac.jpl.nasa.gov/GRACE).

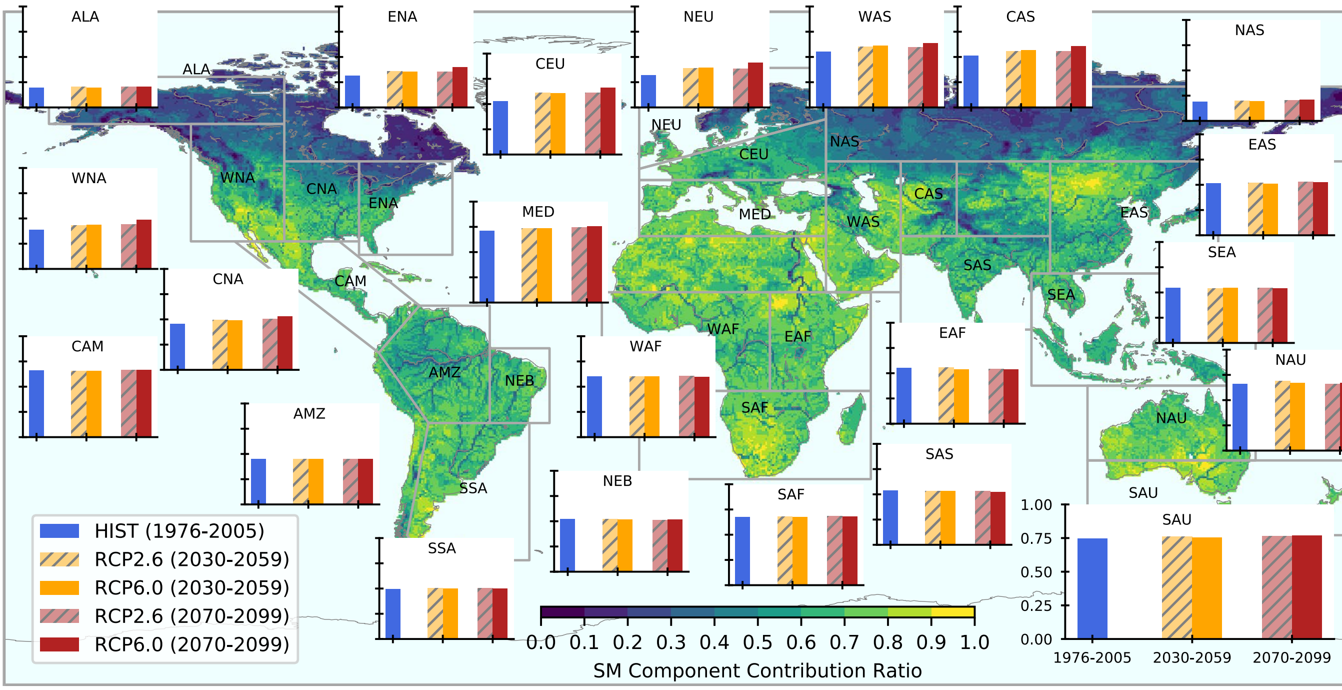

Extended Data Fig. 6 | Soil moisture (SM) component contribution ratio (CCR[16,78]). The background map depicts the spatial variability of SM CCR (the ratio of seasonal amplitude of SM to that of TWS; see Methods) based on the ensemble mean results for the historical baseline period (HIST; 1976–2005). The insets present the SM CCR averaged over the IPCC SREX regions for the historical baseline period, mid-twenty-first century (2030–2059), and late-twenty-first century (2070–2099); results from both RCPs (RCP 2.6 and 6.0) are shown. Evidently, and as discussed in the main text, SM CCR shows a large spatial variability.

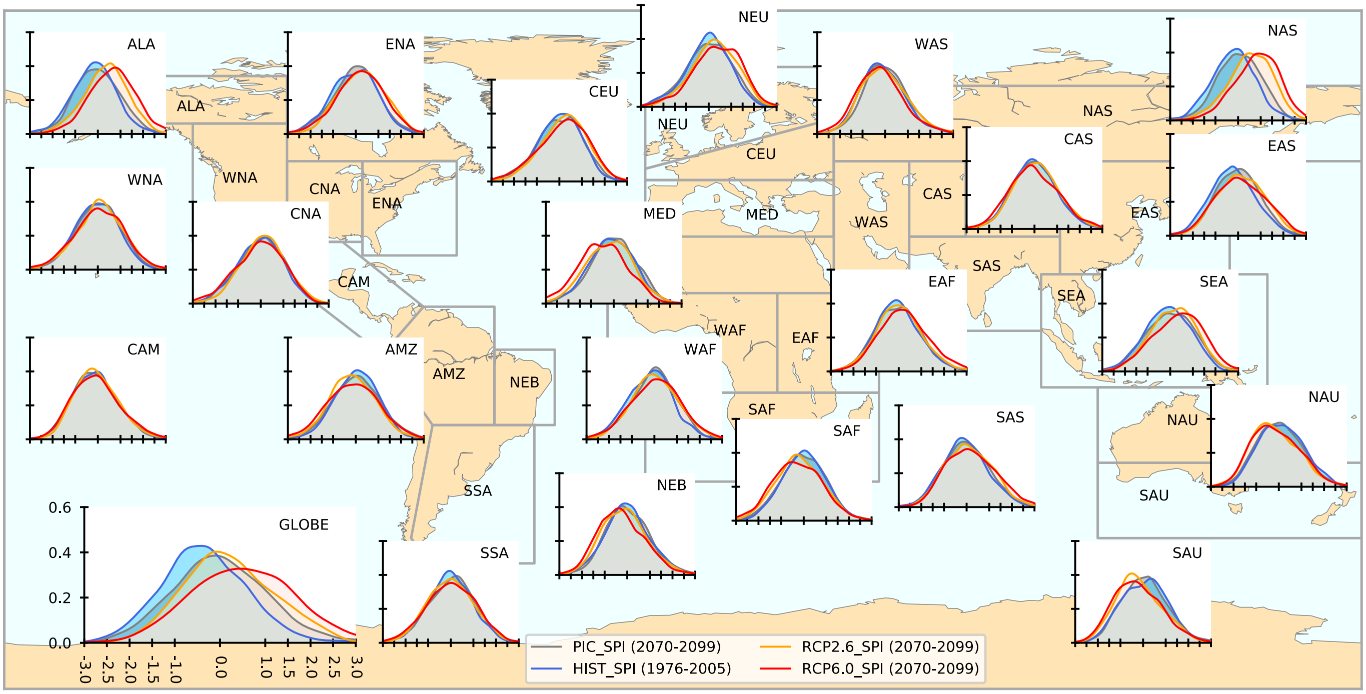

Extended Data Fig. 7 | Probability density function of monthly standardized precipitation index (SPI[29]; see Methods). Shown are ensemble simulations grouped for different cases (that is, HIST, PIC, RCP2.6, and RCP6.0). Labels are indicated in the inset for the entire globe; x-axis labels indicate the SPI. A description of SREX regions (background map) is provided in Supplementary Fig. 3.

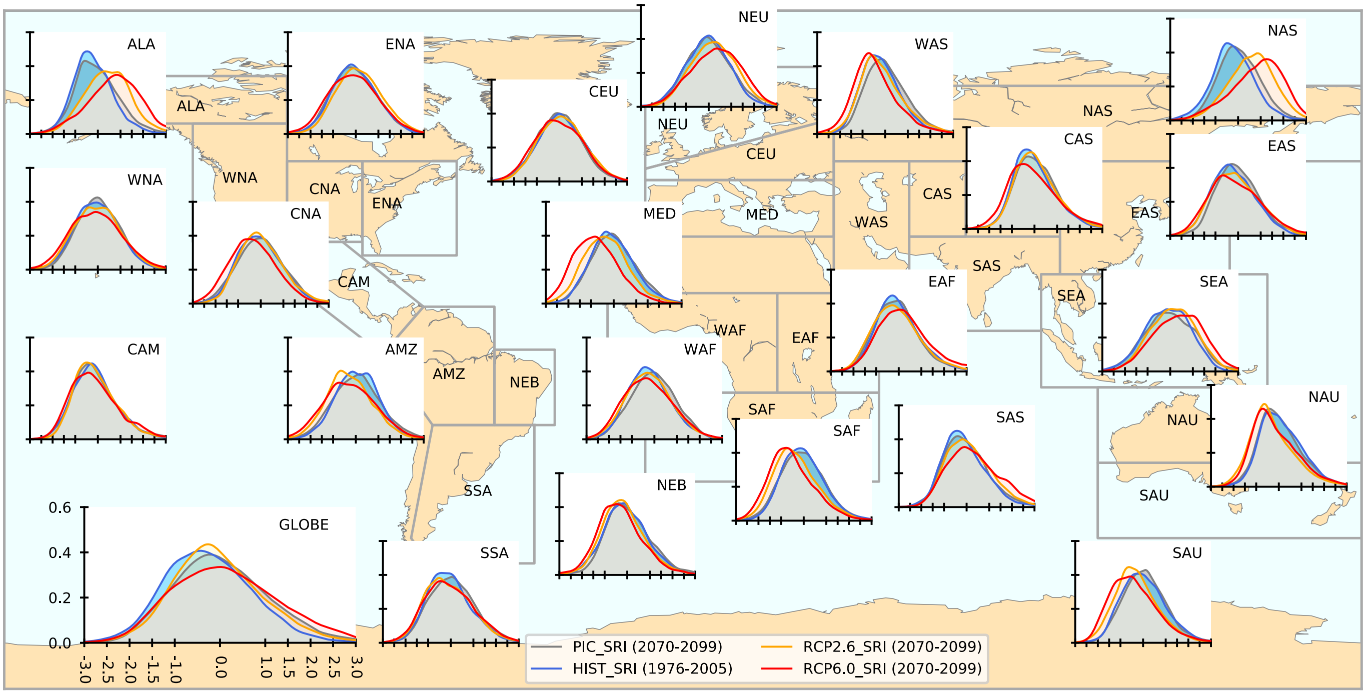

Extended Data Fig. 8 | Probability density function of monthly standardized runoff drought index (SRI[33]; see Methods). Shown are ensemble simulations grouped for different cases (that is, HIST, PIC, RCP2.6, and RCP6.0). Labels are indicated in the inset for the entire globe; x-axis labels indicate the SRI. A description of SREX regions (background map) is provided in Supplementary Fig. 3.

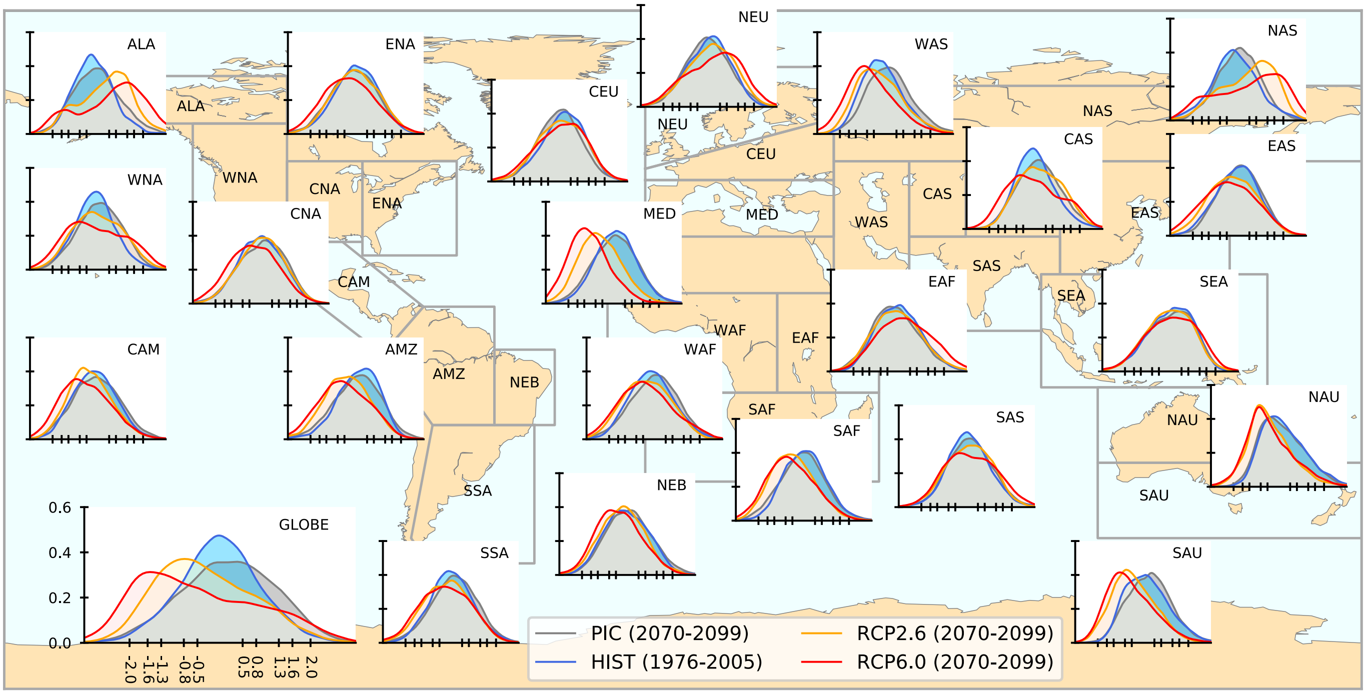

Extended Data Fig. 9 | Probability density function of monthly soil moisture drought index calculated based on Zhao et al. (ref. [5]), that is, by using only soil moisture instead of total TWS. Shown are ensemble simulations grouped for different cases (that is, HIST, PIC, RCP2.6, and RCP6.0). Labels are indicated in the inset for the entire globe; x-axis labels indicate the soil moisture drought index. A description of SREX regions (background map) is provided in Supplementary Fig. 3.

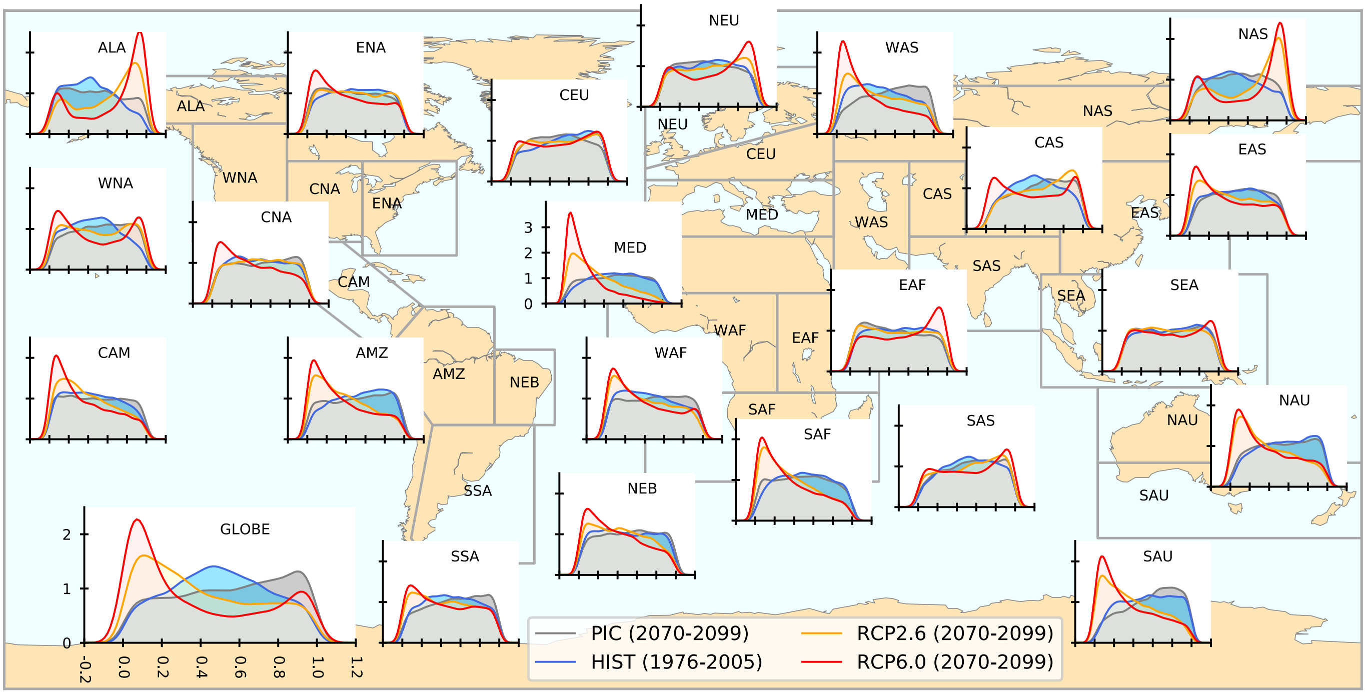

Extended Data Fig. 10 | Probability density function of monthly soil moisture drought index (SMI[31,32]; see Methods). Shown are ensemble simulations grouped for different cases (that is, HIST, PIC, RCP2.6, and RCP6.0). Labels are indicated in the inset for the entire globe; x-axis labels indicate the SMI. A description of SREX regions (background map) is provided in Supplementary Fig. 3. Note the different y-axis scale for MED.